J. Fluid Mech. (1979), *vol.* 93, *part* 4, *pp.* 661–703
Printed in Great Britain

Generation of initial wavelets by instability of a coupled shear flow and their evolution to wind waves

By SANSHIRO KAWAI
Geophysical Institute, Tohoku University, Sendai, Japan

(Received 4 May 1978 and in revised form 16 November 1978)

The generation of initial wavelets, which appear at the initial stage of the generation and growth processes of wind waves after the abrupt start of the wind on a still water surface, has been investigated by systematic experiments together with theoretical analyses. The energy of the initial wavelets, measured by a resistance-type wave gauge of 50 μm diameter, grew exponentially with time at a constant frequency. The frequency and the growth rate were independent of the fetch but did depend on the friction velocity u_{*a} of the air. The phase velocity of the initial wavelets, measured by a shadowgraph-photography technique, was nearly constant, independent of u_{*a}. A coupled shear flow model in the air and water was examined, to explain the observed characteristics of the initial wavelets in terms of the instability mechanism. The theoretical analysis showed that, for each shear flow pattern observed in the experiments, there exist waves whose growth rate is maximum. The frequency, the growth rate and the phase velocity of these critical waves were virtually coincident with those properties of the observed initial wavelets. It is concluded that the generation of wind waves, whose initial stage is called the initial wavelets, is caused by the selective amplification, by the instability mechanism, of the small perturbations which inevitably occur in the flow.

The limitation of the linear instability theory as applied to the process of further growth of the wind waves is also discussed. From some facts recognized through detailed observations, it is inferred that the phenomena controlled by the linear mechanism last for only about 10 s, and that these evolve to the wind waves which are characterized by inherent nonlinearity.

1. Introduction

During the last two decades, Phillips' (1957) resonance mechanism and Miles' (1957*a*) instability mechanism have been referred to, whenever the mechanisms of generation and growth of wind waves are discussed. Turning his attention to the complementary relation between the two mechanisms, Miles (1960) proposed the Phillips–Miles combined mechanism, and thereafter, Miles' mechanism has been considered efficient as the growth mechanism of wind waves, and Phillips' mechanism as the generation mechanism or as the trigger mechanism before Miles' mechanism becomes efficient. In fact, Phillips' mechanism was shown later to be ineffective as the growth mechanism, since the pressure fluctuations in a turbulent atmosphere are much smaller than was originally assumed by Phillips, as pointed out by Stewart (1974). On the other hand, Miles' mechanism was also shown to be ineffective as the

0022-1120/79/4236-7060$02.00

growth mechanism (see, for example, the observation by Snyder & Cox 1966), since the growth rate expected from the theory was far smaller than the observed one. Thus, for the generation stage, Phillips' mechanism has been left without any definite evidence to examine its efficacy. For the growth stage, although some efforts were made to modify Miles' mechanism, for example by taking into account the turbulence in the air, no conclusive results have been obtained.

The results of our recent experiments on the detailed structure of wind waves also strongly suggest that the two current mechanisms are not effective during the growth stage, and demand an entirely different approach in order to investigate the growth mechanism of wind waves. Toba *et al.* (1975) showed that the growing wind waves are accompanied by forced convection relative to the crest of individual waves. These conspicuous structures of wind waves can hardly be represented by a superposition of sinusoidal component waves. Okuda, Kawai & Toba (1977) showed that the stress at the water surface exerted by the wind is maintained almost entirely by the shearing stress concentrated on the windward face near the crest of the individual waves. This fact conflicts with the mechanisms in which the pressure distribution along the water surface plays an essential role in transferring momentum from the wind to the waves. Based on these revelations of strong nonlinearity in the growth process of wind waves, Toba (1978*a*) proposed the stochastic form for the growth of wind waves in a single-parameter representation.

Recently, Larson & Wright (1975) showed, by an observation using microwave backscatter, that the spectral amplitude grows at an exponential rate in the first stage of the development of wind waves. From this fact, it is expected that the initial growth of wind waves is caused by one of the instability mechanisms such as Miles' mechanism, rather than a resonance mechanism as proposed by Phillips. In fact, Valenzuela (1976) applied the shear flow instability theory to a model of two-layer viscous fluids and showed that the growth rate observed by Larson & Wright agrees with that expected from the theory. However, he did not discuss the relation between the observed fact and the generation mechanism itself. In order to discuss the generation mechanism, it is necessary to make measurements of various quantitative properties of waves initially generated with some specific characteristics, and thus to clarify the mechanism which can select the waves having the specific characteristics.

Now we describe, as an introduction, an outline of the time sequence of the phenomena appearing after the abrupt start of the wind on the water surface. A shear flow first starts and grows in the uppermost thin layer of the water, and then the appearance of waves follows several seconds later. The waves which appear initially are long-crested and regular, and so they are distinguished from those appearing later, which are short-crested, irregular and accompanied by forced convection. The distinction between the two kinds of waves is clearly shown in figure 1 (plate 1) which is a sequence of photographs of the water surface. The photographs were taken at about 0·6 s intervals by a camera facing vertically downward.

The work reported here is aimed at revealing the nature of the initially appearing waves and their mechanism of generation. In this report, the initially appearing waves are called the 'initial wavelets' after Kunishi (1963), but with a restricted meaning. Kunishi (1963) used the same terminology to refer also to the waves appearing at short fetches in the fetch-limited case of stationary wind waves. This is due to the fact that the fetch-limited wind waves have many similar aspects to wind waves

which are growing in time, as will be shown later. In the following discussion the term is used to refer only to the latter, but when it is necessary to distinguish them, the former are called the spatial initial wavelets and the latter the temporal initial wavelets.

So far, there has been no systematic study of the temporal initial wavelets, though there have been a few studies on the spatial initial wavelets, such as those of Kunishi (1963) and Plate, Chang & Hidy (1969). The lack of systematic studies on the temporal initial wavelets might have been caused by difficulties in experiment and statistical treatment of data, since the duration of the temporal initial wavelets is very short, as will be described later. In fact, an attempt by Hidy & Plate (1966) failed to clarify the nature of the temporal initial wavelets, because of the limitation of the method of statistical analysis applicable at that time. This is in contrast with the success of Plate *et al.* (1969) in clarifying the nature of the spatial initial wavelets. In their recent work, as was already mentioned, Larson & Wright (1975) succeeded in measuring the temporal growth rate of wind waves in the first stage of their development. One of the reasons for their success was that they overcame the difficulties that Hidy & Plate (1966) encountered in representing the unsteady process of wind waves, by using a new technique to obtain the spatial average of wave energy over the surface area illuminated by the antenna which transmits microwaves. However, they were not able to obtain the continuous spectrum of waves due to another limitation of the new technique. They obtained only the energy growth rate for waves of six fixed wavenumbers. In order to investigate the nature of the initial wavelets, especially their frequency or wavenumber, it is necessary that the time series of their continuous energy spectrum be measured, either in the frequency space or in the wavenumber space. Fortunately, a new method of spectral analysis has been developed in the last decade, which enables us to calculate the time series of the continuous spectrum of wind waves including initial wavelets. The experimental procedures will be described in § 2 and the methods of data analysis and the results in § 3.

The results of the experiment are suggestive of a certain instability mechanism for the generation of initial wavelets. Therefore, a shear flow model of the flow in the air and water is examined, to explain the observed nature of the initial wavelets in terms of the instability mechanism which will be formulated in § 4. Numerical procedures to solve the problem will be described in § 5. This model is taken as the generation mechanism of initial wavelets, as will be described in § 6.

2. Experimental apparatus and measuring instruments

2.1. *Wind-wave tunnel*

The experiments have been made with a wind-wave tunnel 60 cm in width, 20 m in length and 120 cm in height, containing water of 70 cm in depth. A schematic picture is shown in figure 2. A gap between the mean water level and the inlet junction plate is smaller than 2 mm; therefore no notable disturbances of water surface were created at the junction between the plate and the water surface. At the downstream end of the tank, a permeable-type wave absorber is installed. An axial fan installed at the upstream end controls the wind speed, which may be changed continuously from 0 to 18 m s^{-1}. The air flow is made uniform by a honeycomb, four fine mesh screens made of steel wire and twenty-four coarse mesh grids made of hemp yarn in the inlet duct. The mesh size of the screens is $2{\cdot}5 \times 2{\cdot}5$ mm and the diameter of the wire is 0·3 mm,

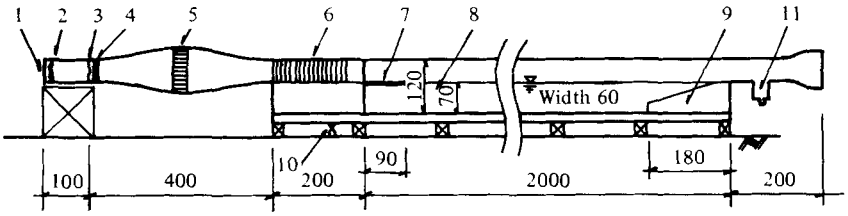

FIGURE 2. Schematic sketch of the wind-wave tunnel. 1, Shutter; 2, blower; 3, flexible joint; 4, fine mesh screens; 5, honeycomb; 6, coarse mesh grids; 7, junction plate; 8, water tank; 9, wave absorber; 10, water inlet (outlet); 11, water outlet for water surface cleaning. The units are centimetres.

and for the grids, these values are 60×70 mm and 2 mm, respectively. To eliminate the influence of the vibration of the fan and motor unit on the measurements, the unit is installed on a vibration-isolated frame with rubber shoes and connected to the wind-wave tunnel by a flexible joint made of canvas. To realize the condition of an abrupt start of the wind, a shutter is placed at the intake of the fan. The shutter can be abruptly opened after the rotation of the fan becomes stable. An event mark was recorded simultaneously on a chart recording signals from wave gauges, by an electric switch placed at the shutter, at the time when the shutter was fully opened. The time indicated by the event mark is the origin of the time co-ordinate throughout the following discussion. In order to remove surface films of contaminant, the surface was cleaned by overflowing the water using the addition of water from the bottom together with a gentle wind, and also by blowing off the surface films with strong wind, at suitable intervals during the experiments.

2.2. *Measuring instruments for the initial wavelets*

Initial wavelets were measured by a resistance-type wave gauge of a single platinum wire of diameter 50 μm. The gauge is built in a bridge circuit designed by Kunishi (1959). The bridge circuit with the gauge is connected to a dynamic strain meter of a standard type, which consists of an oscillator of carrier, a discriminator and an amplifier. Mitsuyasu & Honda (1974) used a similar system to measure the high frequency spectrum of wind waves, and showed that the amplitude response factor for a single platinum wire gauge with a diameter 100 μm is approximately unity up to 80 Hz, with a careful and skilful measurement. As the amplitude response factor of this kind of wave gauge mainly depends on the thickness and material of the wire, the amplitude response factor of the present wave gauge for measuring initial wavelets is safely expected to be unity up to 80 Hz.

A long period variation of water level was seen due to the set-up by the wind, especially at the start of the experiment, as shown in figure 3 which is a trace of an oscillograph chart. To prevent the long period variation bringing the signal over the measuring limit of recorder, another signal was also recorded through a high-pass filter of 3 Hz cut-off frequency, as shown in figure 3. The oscillation of about 2 Hz, seen in the trace of the filtered signal before the sudden appearance of the initial wavelets, is expected to be the lateral oscillation of the water in the tank.

Figure 4 shows an example of the calibration curve of the wave gauge. A linear relation is seen up to about 3 cm in the change of water level. The maximum variation of water level in the main parts of the present experiments was about 5 mm, including

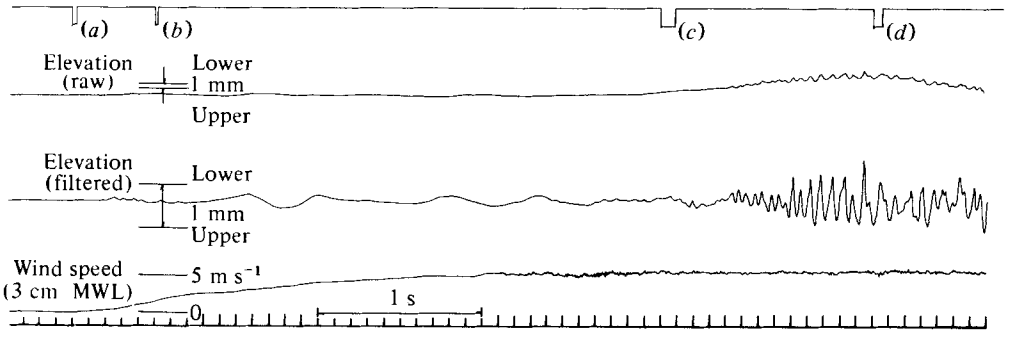

FIGURE 3. A trace of an oscillograph chart showing, from the top to the bottom, event marks, direct signal of wave gauge, filtered signal of wave gauge, wind speed measured with a hot-film anemometer at height 3 cm above the mean water level and 0·1 s time marks. Event marks: (*a*) the time when the shutter begins to open; (*b*) the time when the shutter is fully opened, being the origin of the time co-ordinate in the present study; (*c*) the time when the initial wavelets are observed with the naked eye for the first time; (*d*) the time when the appearance of water surface changes from regular to irregular for the naked eye. The event marks (*a*) and (*b*) are automatically entered with a switch placed at the shutter. The event marks (*c*) and (*d*) are manually entered with a switch in the hand. $F = 9$ m; $U_r = 6{\cdot}9$ m s^{-1}.

the long period variation due to the set-up by wind; consequently, the whole range was within the linear range of the calibration.

Since the wave height of the initial wavelets is very small, the water level resolution of the wave gauge is also important. Figure 5 shows another example of the calibration curve of the wave gauge when the water level is changed in steps of 26·2 μm which is the minimum value of our apparatus for calibrating the wave gauge. It can be said, from the figure, that the resolution of the wave gauge is better than 26·2 μm.

It should be noted that the methods of recording and digitizing the output signal from the wave gauge are different in the two series of experiments I and II, of which the details will be described in the next section. In I the signal was recorded on an electromagnetic oscillograph whose response factor is unity up to 750 Hz, and digitized manually with a scale rule. In II the signal was recorded on an FM magnetic tape recorder whose response factor is unity up to 500 Hz, and digitized automatically by an a.d. converter. For both cases, the noise level is estimated to be lower than 1 % of the signal level.

To measure the phase velocity of the initial wavelets, a method of shadowgraph-photography devised by Koga & Toba† was used. The images reflected by a mirror which was placed at the bottom of the water tank at an angle of 45° with the bottom plate, were photographed by a 16 mm cinecamera which was directed horizontally and perpendicularly to the side wall of the tank made of glass plates. A tracing paper to illuminate the background of the view was placed on the upper cover of the wind-wave tunnel which was made of transparent acrylate resin, and illuminated by a stroboscope synchronized with the shutter of the cinecamera. The phase velocity of the initial wavelets was estimated from adjacent frames, by measuring the distance travelled by certain crests during the time between successive frames. These pictures were not used to measure the wavelength of the initial wavelets, becasue they were too scanty in number to determine reliable values of wavelength from them.

† Study on the distribution of water droplets produced on wind-wave surface (to be published).

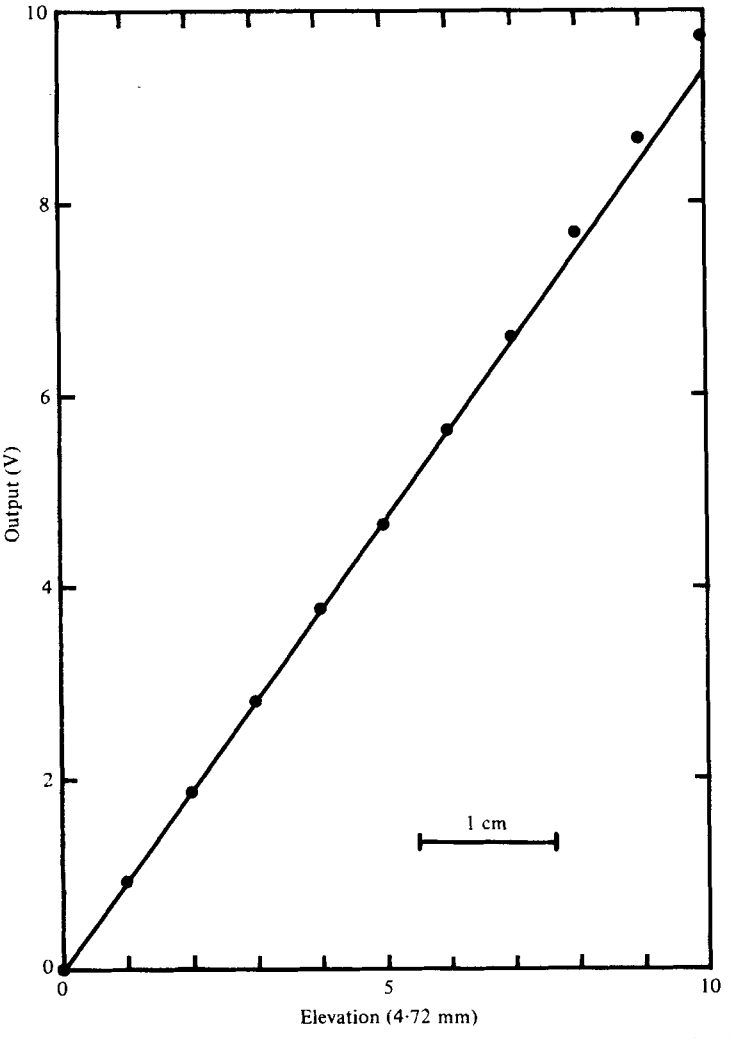

FIGURE 4. Linear calibration of the wave gauge. The unit of the abscissa is the step of immersion of the wave gauge.

2.3. *Measuring instruments for flows in water and air*

The flow in the water was measured by flow visualization techniques, which were reported in detail by Okuda *et al.* (1976) with several photographs. In brief, hydrogen bubble lines produced by the electrolysis of water were emitted from a 50 μm platinum wire which was stretched vertically through the interface, and they were photographed by a 16 mm cinecamera as tracers of flow in the water. The instantaneous velocity profile was estimated by measuring the vertical distribution of the distance between adjacent bubble lines and dividing the distance by the interval at which the hydrogen bubble lines were emitted by an electric pulse generator. It is noteworthy that, in the process of the estimation of the velocity profiles, they were corrected by the ascent velocity of bubbles which was measured separately. Not only the velocity profiles, but also the wind stress exerted at the interface, may be determined with the

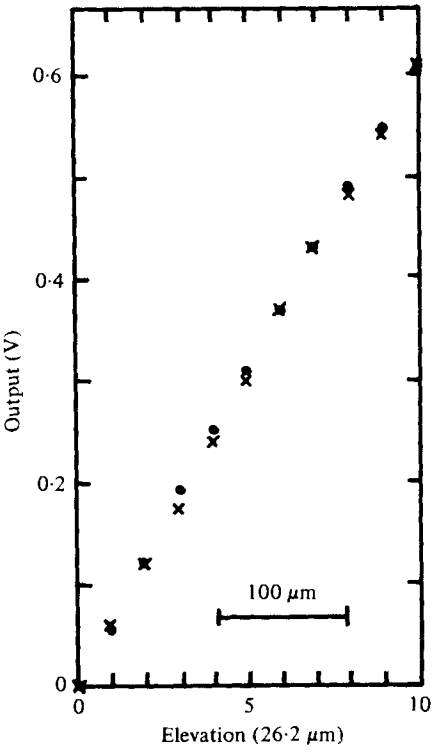

FIGURE 5. A calibration for the resolution of the wave gauge. The wave gauge is moved downward (●) or upward (×) in steps of 26·2 μm, which is the minimum value of our apparatus for calibrating the wave gauge.

method. The wind stress measured at the initial stage of the development of wind waves, as will be described later, is much smaller than that determined when wind waves are in a fully developed state, and it seems almost impossible to estimate the former with other methods such as profile measurements of this air flow, since the conditions are varying temporally within a very thin boundary layer.

In order to measure the flow in the air, three kinds of instruments were used. The first is a hot-film anemometer for measuring the rising stage of the wind speed at the start of the wind. An example of the record is shown in figure 3. The second is a Pitot-static tube and a pressure-difference meter for measuring the wind profile in the steady state. The third is a photoelectric-type windmill anemometer installed at the inlet of the tunnel for measuring the wind speed in the steady state, and this value is used in this paper as the reference wind speed U_r to represent the experimental conditions.

3. Results of the experiment

3.1. *Properties of initial wavelets in I*

Two series of experiments were carried out. The first, I, was made to examine the characteristics of the initial wavelets in relation to the wind speed and the fetch. The number of experimental cases is twenty and their conditions are listed in table 1,

Fetch (m)	U_r (m s^{-1})	u_{*w} (cm s^{-1})	u_{*a} (cm s^{-1})
3	4·2	0·56	15·8
	5·0	0·61	17·2
	5·6	0·71	20·0
	6·3	0·73	20·5
	6·9	0·88	24·8
	7·7	0·95	26·8
6	4·2	0·52	14·6
	5·0	0·63	17·7
	5·6	0·67	18·9
	6·3	0·72	20·3
	6·9	0·85	23·9
	7·7	0·89	25·0
	8·4	1·00	28·1
9	4·2	0·47	13·1
	5·0	0·61	17·0
	5·6	0·66	18·4
	6·3	0·75	20·9
	6·9	0·82	22·9
	7·7	0·90	25·1
	8·4	1·01	28·2

TABLE 1. Conditions of experiment I.

where U_r is the reference wind speed measured at the centre of the inlet section, u_{*w} the friction velocity of the water at the interface determined from the velocity profile of the water flow measured at the time when the initial wavelets are seen, and u_{*a} the friction velocity of the air determined from u_{*w} assuming the continuity of the shearing stress at the interface. In the following discussion, these values of u_{*a} are used as the values of friction velocity relating to the generation and growth processes of initial wavelets. The slight inequality referred to the fetch, seen in the values under the same reference wind speed, seems to be caused by some indefiniteness in determining u_{*w} through averaging the scattered values each of which is estimated from the instantaneous velocity profiles, rather than by the fetch-dependency of the friction velocity. More detailed descriptions of u_{*w} will be given later in § 3.3.

To represent the generation and growth processes of initial wavelets, wave data were divided into many segments of carefully chosen length, and the power spectrum was calculated for each segment under a hypothetical condition of quasi-steady state, to construct the time series of the power spectra at adequate intervals. In order to take reliable spectra with sufficient resolving power, the length of the divided data must be long. On the other hand, it must be short, in order to express properly the unsteadiness of the process. The two opposing necessities cannot be reconciled by conventional methods of spectral analysis. This is the difficulty that Hidy & Plate (1966) encountered. A new method of spectral analysis, originated by Burg (1967), called maximum entropy method (MEM), has been developed in the last decade. Since the method makes it possible to calculate reliable spectra with certain resolving power from relatively short data, the above-mentioned difficulty can be overcome by use of this method. Strictly speaking, we used Akaike's (1969) method for the estimation of

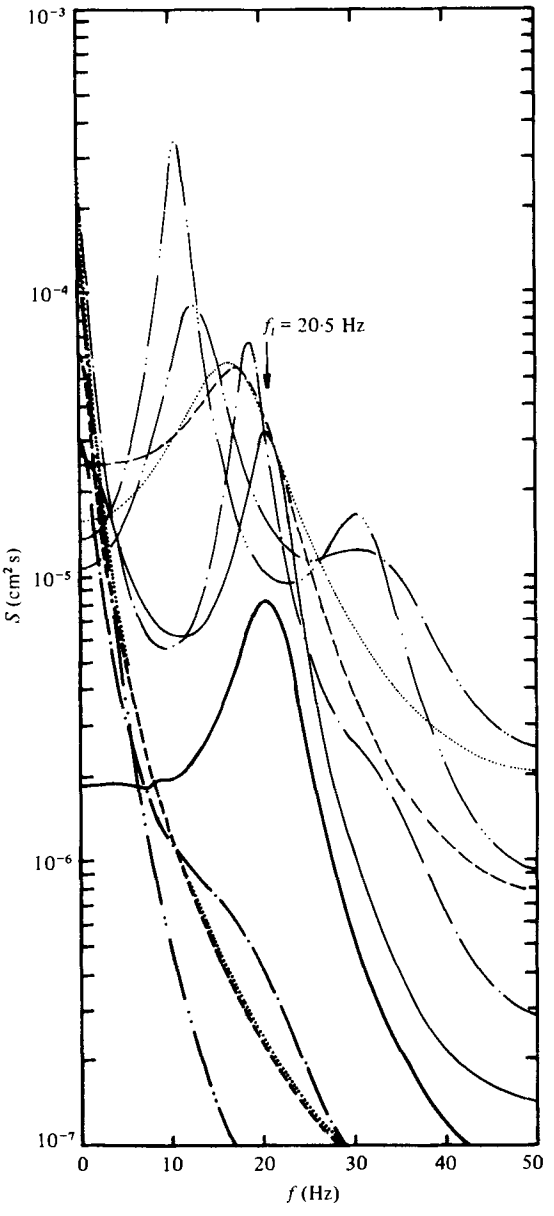

FIGURE 6. A time series of power spectra for a case of experiment I. f_i is the frequency of initial wavelets. The conditions of the data analysis: digitizing interval Δt = 0·01 s; data number per sample N = 50; maximum lag number L = 20; the number of samples averaged for one spectrum NS = 1. FPE criterion is used. F = 3 m; U_τ = 6·9 m s^{-1}. The various ranges of t (s) are: —··—, 2·0–2·5; ·····, 2·25–2·75; – – – –, 2·5–3·0; —·—, 2·75–3·25; ——, 3·0–3·5; —— 3·25–3·75; —·—, 3·5–4·0; – – – –, 3·75–4·25; ·····, 4·0–4·5; —··—, 4·25–4·75; —···—, 4·5–5·0.

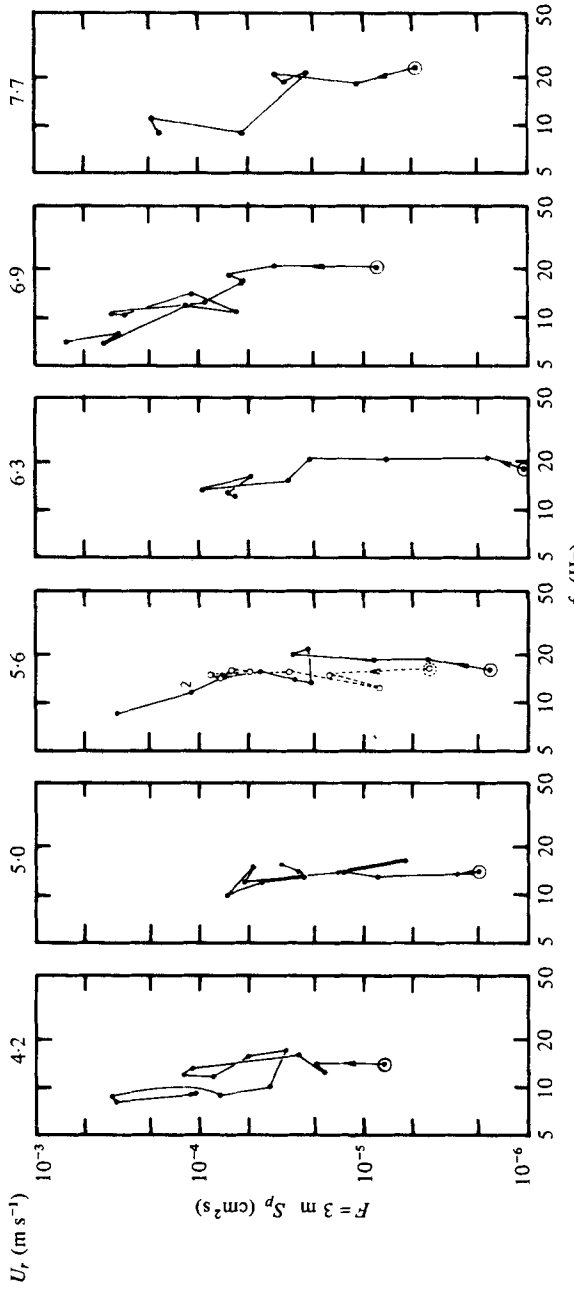

FIGURE 7. For legend see p. 672.

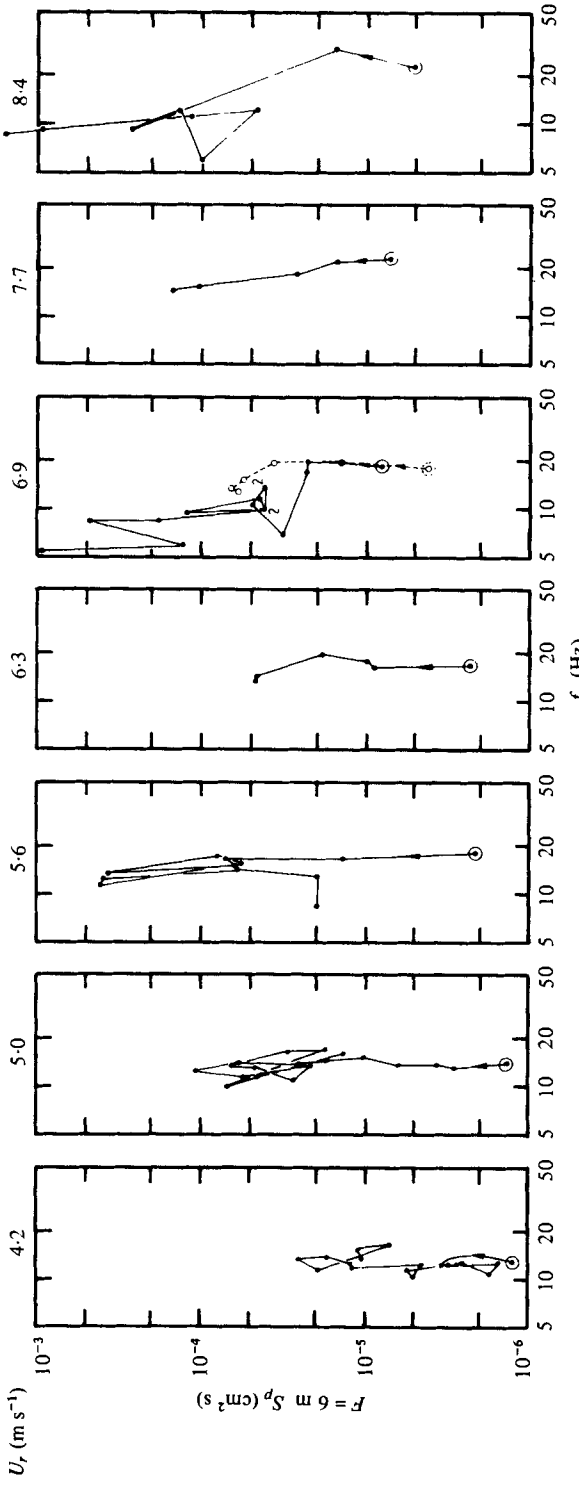

FIGURE 7. For legend see p. 672.

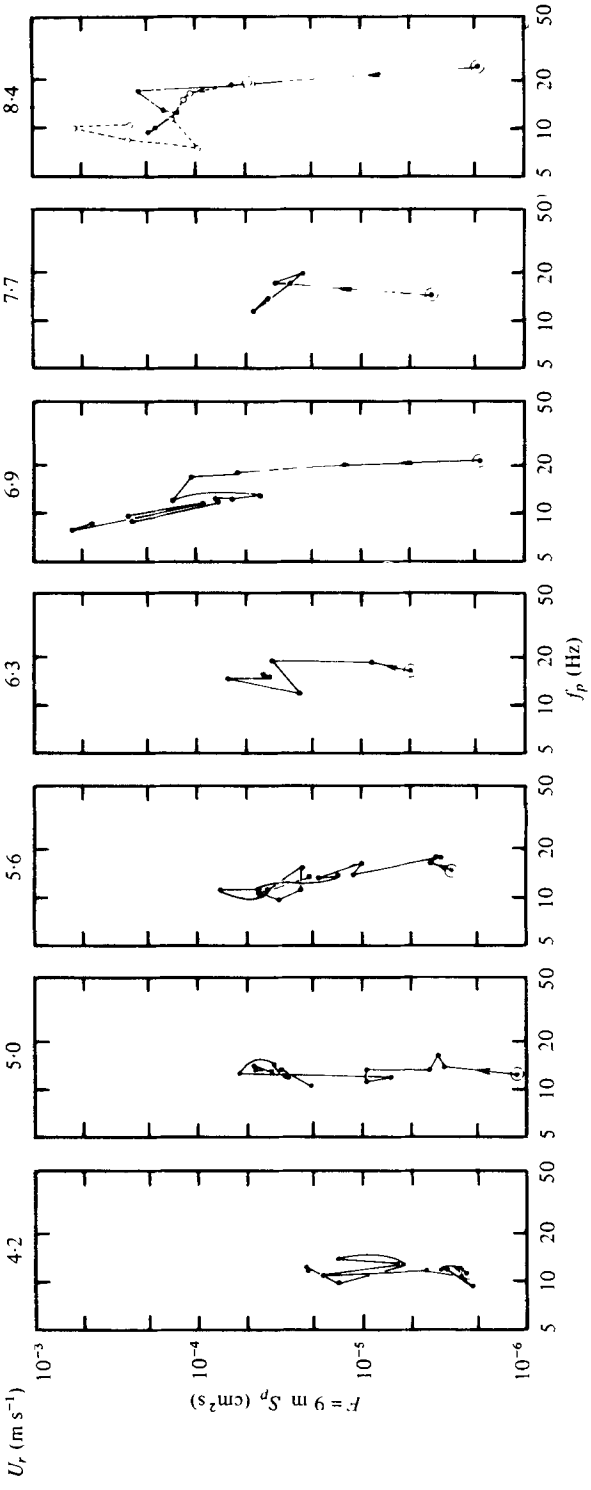

FIGURE 7. Time series of the spectral peak after the first appearance of initial wavelets for all cases of I. The time of first appearance is indicated by double circle for each case. The interval between successive points is 0·25 s. The conditions of the data analysis are the same as figure 6. The two time series in three figures represent the duplication of experiment. Points with a figure 2 represent the fact that there is a spectrum without significant peaks at the succeeding sampling time.

power spectra through an autoregressive model, which was shown to be identical with MEM by Ulrych & Bishop (1975).

The wave data analysed in the present study are those passed through the electric high-pass filter. The conditions of the data analysis in I are as follows. The digitizing interval is 0·01 s, data number per sample 50, the calculating interval of spectra 0·25 s, the maximum lag number 20, and the order of autoregressive model is decided from the condition that the final prediction error (FPE) becomes minimum, according to Akaike (1970). In figure 6 is shown an example of time series of power spectra. We may recognize from the figure that there are two stages in the evolution of the spectrum. In the first stage, the frequency f_i of the spectral peak is kept nearly constant and its energy increases with time. Then in the second stage, the decrease of the frequency commences and the increase of energy is not necessarily monotonic, although the energy increases statistically with time. These tendencies are similar to those seen in the sequence of the power spectra of fetch-limited wind waves observed by Plate *et al.* (1969), and the fact shows that the qualitative description by Kunishi (1963) is correct about the similarity between the temporal and spatial growth processes of wind waves. Those waves with a constant frequency which appear at the first stage of development are the waves termed initial wavelets. It should be noted here that the spectral density function obtained in the present study by the analysis with MEM is continuous in the region of frequency from zero to the Nyquist frequency; consequently the frequency of the initial wavelets can be decided minutely.

Those general tendencies are seen in all cases of the experiment as shown in figure 7; except the cases of lower wind speeds in which the spectral analysis is made only in the earlier stage of the development and the decrease of the frequency of the spectral peak is not necessarily clear. The figure shows the time series only of the spectral peak. The plots start from the double-circle point at the bottom and, for each case, move upward keeping approximately the same value of f_i; they then move left and upwards in a more or less irregular manner. For each of three cases the experiment was carried out twice; these are shown simultaneously in the figure with different symbols, that is, a solid line and a broken line. In the figure, points with a figure 2 indicate that there is a spectrum without significant peaks at the succeeding sampling time.

Figure 8 shows the correlation of the frequency f_i of the initial wavelets with u_{*a} for all cases of experiment I by symbols of solid circles, semi-solid circles and open circles, for three fetches 3, 6 and 9 m, respectively. It is seen that f_i is apparently dependent on u_{*a} but independent of the fetch, although the points are rather scattered, presumably because only a single experiment at each point is not necessarily representative. In figure 8 the frequency of the spatial initial wavelets measured by Plate *et al.* (1969) is shown by plus symbols. As to the cause of the apparent difference between the frequencies of the two kinds of initial wavelets, this will be discussed in § 6.

Figure 9 shows the correlation of the energy growth rate β of the initial wavelets with u_{*a} for all cases of I with the same symbols as in figure 8. The values β are decided from the gradient of the straight lines of best fit drawn in the figures correlating the logarithm of the energy density of the spectral peak with the time. Although the points in figure 9 are more scattered than in figure 8, it is seen that β is also dependent on u_{*a} but independent of the fetch.

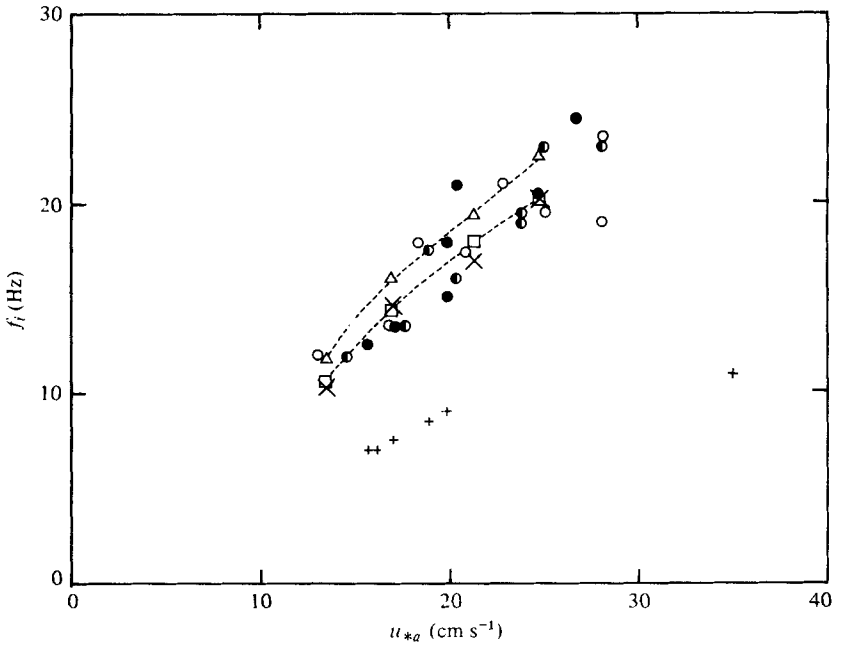

FIGURE 8. Correlation between u_{*a} and the frequency f_i of the observed initial wavelets together with the frequency of the waves whose theoretical growth rate by the two-layer model is maximum. Observed values by Plate *et al.* (1969) are those of spatial initial wavelets (+). Experiment I: ●, $F = 3$ m, $NS = 1$; ◐, $F = 6$ m, $NS = 1$; ○, $F = 9$ m, $NS = 1$. Experiment II: ×, $F = 8$ m, $NS = 8$. Theory: □, $U_1/u_{*a} = 5{\cdot}0$; △, $U_1/u_{*a} = 8{\cdot}0$.

3.2. *Properties of initial wavelets in II*

To make the spectra more reliable, four series of experiments were carried out in II, each of which consists of eight experiments under a fixed condition. In order to estimate the frequency f_i and the growth rate β of the initial wavelets, the time series of the average spectra of the eight samples were constructed for each experimental condition. Since f_i and β of the initial wavelets are independent of the fetch, as shown in I, the experiments were made at a fixed fetch of 8 m, for four wind speeds. The wind conditions are shown in table 2, where the same items as in table 1 are listed, together with the maximum wind speed U_m and the friction velocity of the air $u_{*a,st}$ which was determined from the wind profile at the fetch of experiment in the steady state after the wind waves became fully developed. It is noteworthy that not only $u_{*a,st}$ but also 0·05 times the representative wind speed such as U_r or U_m is much greater than u_{*a} which was measured at the same time as the first appearance of initial wavelets. The fact shows that Valenzuela (1976) overestimated the friction velocity of the air at the initial stage of development of wind waves, since he used the factor 0·05 to estimate the friction velocity from the representative wind speed observed by Larson & Wright (1975), although the difference between the wind-wave tunnels may introduce some uncertainty to the argument.

Figure 10 shows, as an example from II, a sequence of spectra throughout the generation and growth processes of wind waves, or from the initial wavelets to the wind waves in their statistically stationary state. As to the conditions of the data analysis, there is a difference in the sampling time referred to the time from the start

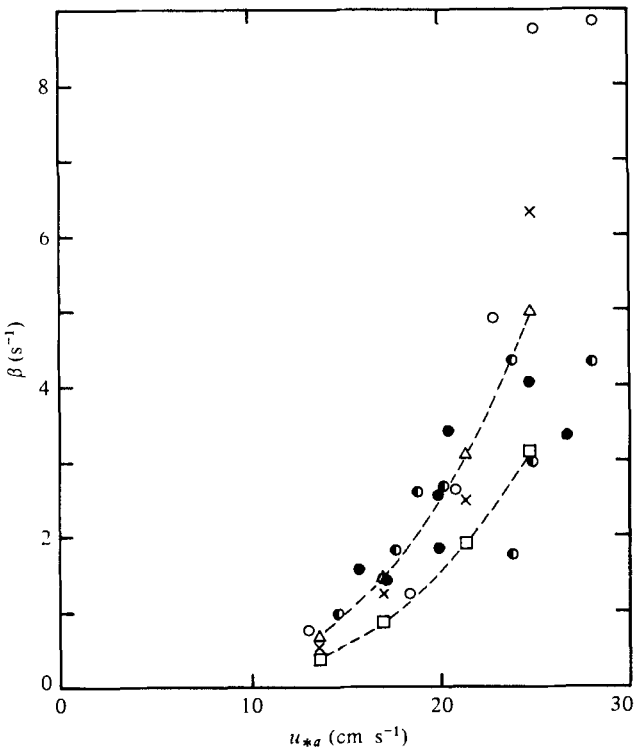

FIGURE 9. Correlation between u_{*a} and the growth rate β of the observed initial wavelets together with the theoretical maximum growth rate by the two-layer model. Symbols as in figure 8.

U_r (m s^{-1})	u_{*w} (cm s^{-1})	u_{*a} (cm s^{-1})	U_m (m s^{-1})	$u_{*a,st}$ (cm s^{-1})
4·2	0·47	13·6	4·3	18·3
5·1	0·59	17·0	5·5	24·9
6·3	0·74	21·4	6·9	42·8
7·4	0·86	24·8	8·1	59·3

TABLE 2. Conditions of experiment II.

of the wind as shown in the figure, where Δt is the digitizing interval, N the number of data per sample and NS the number of samples averaged to calculate one spectrum. Maximum lag number L may be computed by an equation $L = 2\sqrt{N}$, after Akaike & Nakagawa (1972). The FPE criterion is used to decide the order of autoregressive model.

From the figure it can be seen, besides the general tendency described by figure 6, that the spectral form at the higher-frequency side of the spectral peak is steeper and more smooth for the spectra of the initial wavelets than for those of the later wind waves. We do not, however, discuss the problem further, because accumulation of data is necessary in order to define the spectral form. The conspicuous lower-frequency

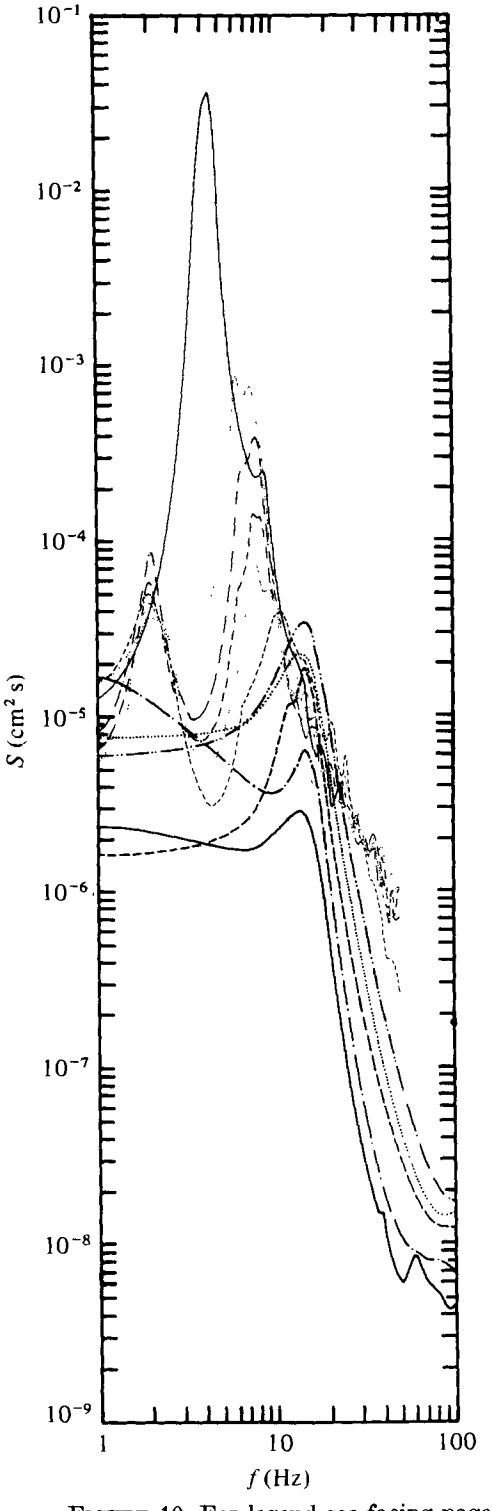

FIGURE 10. For legend see facing page.

peak seen in the spectra of the developing wind waves is due to the lateral oscillation of the water in the tank. When the initial wavelets were analysed, this oscillation had been reduced from the data with the Fleck & Fryer (1953) numerical filter that filters off half of the energy at 2 Hz. It is noteworthy that the time when the spectral peak frequency starts to wander from the frequency of the initial wavelets, coincides well with the time when the wave surface changes from regular state to irregular. The time of the visual change of the surface was also recorded manually with a marker switch simultaneously in the electromagnetic oscillograph or the monitoring pen-writing oscillograph, as shown in figure 3.

Figure 11 shows the sequences of the spectra of initial wavelets for all cases of II from the generation of initial wavelets to the time when the spectral peak frequency starts to wander. The case shown in figure 10 corresponds to figure 11(*b*). The conditions of the data analysis are shown in the figure, except the common conditions which are the equation $L = 2\sqrt{N}$ and the FPE criterion to decide the order of autoregressive model. Generally, the frequency of the initial wavelets is remarkably stable, demonstrating clearly the existence of initial wavelets with a constant frequency. The frequency f_i is about 10·5 Hz for the case $U_r = 4{\cdot}2$ m s^{-1}, although there exist spectra having multiple peaks other than the second harmonics of the initial wavelets, including a peak at the low-frequency side. The energy at low-frequency was caused by the residual long period undulation and the lateral oscillation leaked from the electric high-pass filter and the numerical high-pass filter. For the case $U_r = 5{\cdot}1$ m s^{-1}, f_i is most stable and 14·5 Hz. For the case $U_r = 6{\cdot}3$ m s^{-1}, f_i is about 17·0 Hz, although there is a slight trend toward a lower frequency with time. For the case $U_r = 7{\cdot}4$ m s^{-1}, f_i is about 20·5 Hz, although there are only two spectra since the duration of initial wavelets is very short. These values of f_i are shown in figure 8 (denoted by the symbol $\times$) as a function of u_{*a}. There is no systematic difference between I and II in the correlation of f_i with u_{*a}.

The growth of the energy of initial wavelets with time is shown in figure 12 for all cases of II. An exponential growth law holds up to a certain time. The values of the growth rate β estimated from the gradient of the lines drawn in the figure are also shown, and their correlation with u_{*a} is shown in figure 9 by the same symbol as in figure 8. It should be noted here that the points plotted in the counterparts of figure 12 for I are more scattered than in figure 12, and consequently, the determination of the values of β was less precise than in figure 12. It seems that the slight difference between I and II in the correlation of β with u_{*a} is caused by this, and that the values of the growth rate in II are more reliable than those of I.

As for the phase velocity of the initial wavelets, the observation was made only for the cases in II and not for the cases in I. The determination was performed only once

---

LEGEND TO FIGURE 10

FIGURE 10. A sequence of spectra from the initial wavelets to the stationary wind waves for a case of II. The equation $L = 2\sqrt{N}$ and FPE criterion are used. $U_r = 5{\cdot}1$ m s^{-1}. Initial wavelets, $\Delta t = 0{\cdot}005$ s, $N = 128$, $NS = 8$, ranges for t (s) are: ——, 8·00–8·64; —·—, 8·64–9·28; — — —, 9·28–9·92; ·····, 9·92–10·56; —··—, 10·56–11·20. Developing wind waves, $\Delta t = 0{\cdot}01$ s, $N = 512$, $NS = 8$, ranges for t (s) are: — — —, 10·24–15·36; ·····, 12·80–17·92; —·—, 15·36–20·48; —··—, 17·92–23·04; ····· ····· ·····, 20·48–25·60. Steady wind waves, $\Delta t = 0{\cdot}02$ s, $N = 1664$, $NS = 1$, the range for t is 40·96–74·24 s (——).

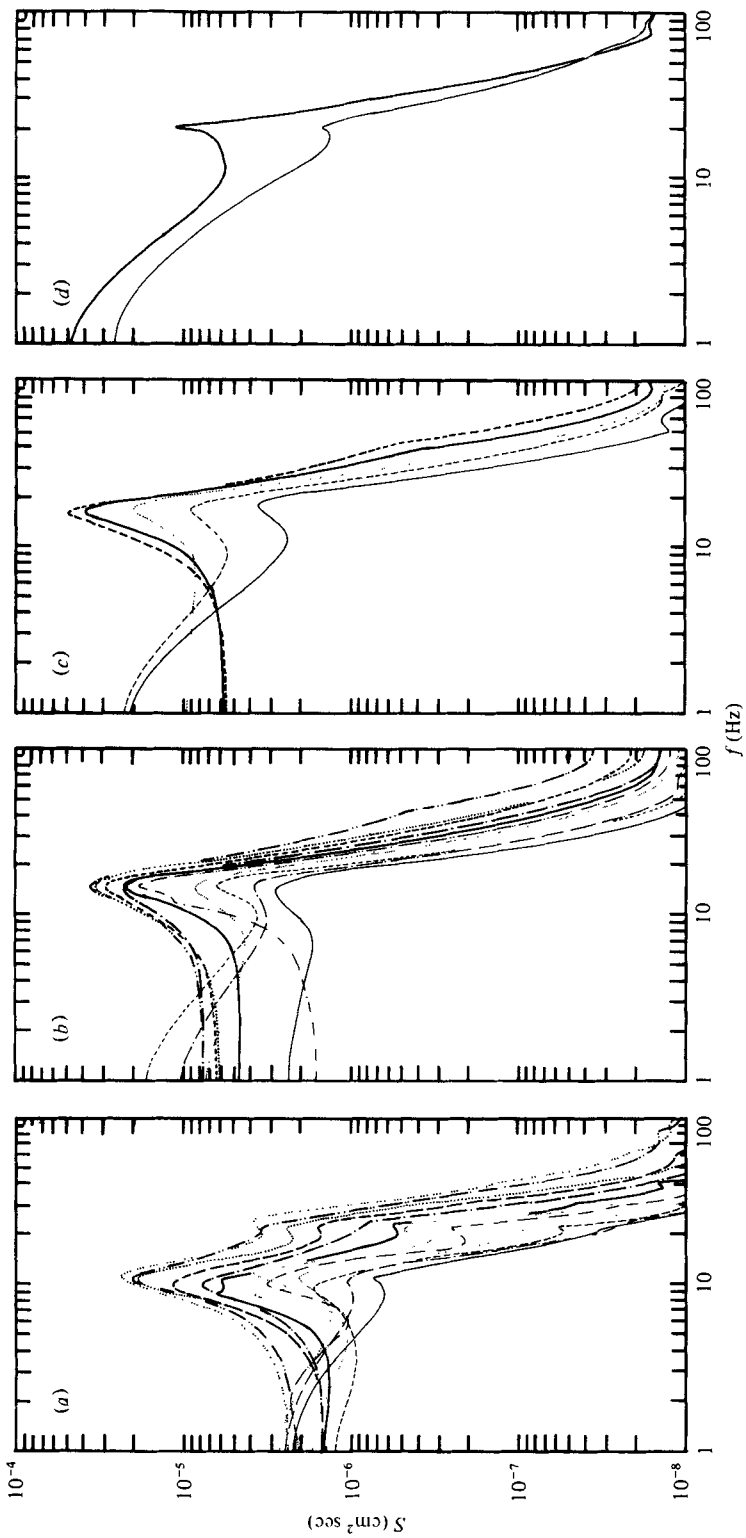

FIGURE 11. Time series of the spectra of initial wavelets for all cases of II. $NS = 8$. The equation $L = 2\sqrt{N}$ and FPE criterion are used. (*a*) $U_r = 4{\cdot}2$ m s^{-1}, $\Delta t = 0{\cdot}005$ s, $N = 256$, ranges for t (s) are: ——, 12·16–13·44; —·—, 12·80–14·08; – – – –, 13·44–14·72; ·····, 14·08–15·36; —·—·—, 14·72–16·00; ·····, 15·36–16·64; ——, 16·00–17·28; —·—, 16·64–17·92; – – – –, 17·28–18·56; ·····, 17·92–19·20; —·—·—, 18·56–19·84; ·····, 19·20–20·48. (*b*) $U_r = 5{\cdot}1$ m s^{-1}, $\Delta t = 0{\cdot}005$ s, $N = 128$, ranges for t (s) are: ——, 8·00–8·64; —·—, 8·32–8·96; – – – –, 8·64–9·28; ·····, 8·96–9·60; —·—·—, 9·28–9·92; ——, 9·60–10·24; —·—, 9·92–10·56; – – – –, 10·24–10·88; ·····, 10·56–11·20; —·—·—, 10·88–11·52. (*c*) $U_r = 6{\cdot}3$ m s^{-1}, $\Delta t = 0{\cdot}005$ s, $N = 128$, ranges for t (s) are: ——, 5·12–5·76; – – – –, 5·44–6·08; ·····, 5·76–6·40; ——, 6·08–6·72; – – – – –, 6·40–7·04. (*d*) $U_r = 7{\cdot}4$ m s^{-1}, $\Delta t = 0{\cdot}005$ s, $N = 128$, the ranges for t (s) are: ——, 3·20–3·84; ——, 3·52–4·16.

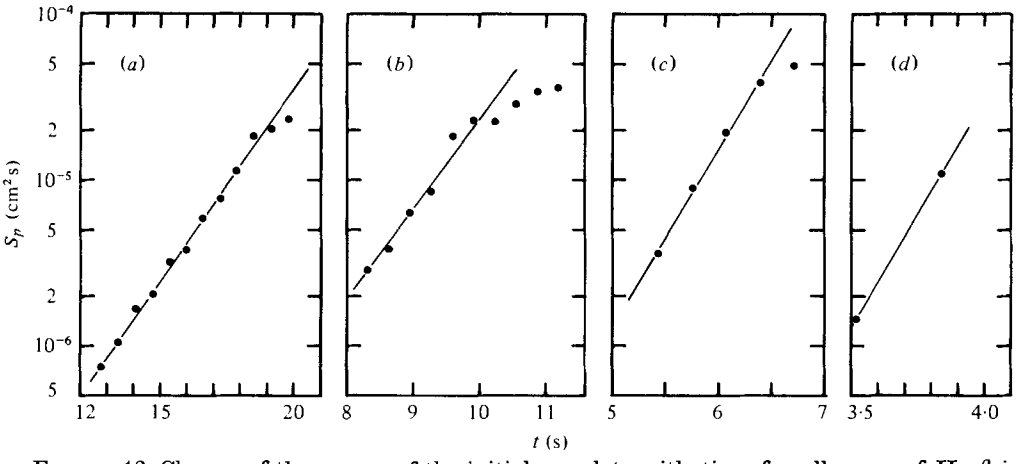

FIGURE 12. Change of the energy of the initial wavelets with time for all cases of II. β is the exponential growth rate of energy. (*a*) $U_r = 4{\cdot}2$ m s^{-1}, $\beta = 0{\cdot}53$ s^{-1}; (*b*) $U_r = 5{\cdot}1$ m s^{-1}, $\beta = 1{\cdot}25$ s^{-1}; (*c*) $U_r = 6{\cdot}3$ m s^{-1}; $\beta = 2{\cdot}47$ s^{-1}; (*d*) $U_r = 7{\cdot}4$ m s^{-1}, $\beta = 6{\cdot}33$ s^{-1}.

for each case of the experiment, because the phase velocity of the initial wavelets is decided from a single observation much more definitely than their frequency or wavenumber. The results will be shown in § 6.

Direct comparison of our results with those of Larson & Wright (1975) is impossible, since they did not refer to the initial wavelets. However, since the initial wavelets are the waves whose growth rate is maximum, as will be shown later theoretically, and they obtained the relation between the growth rate and the wavenumber, we can, to some extent, show consistency between the two experiments; however, we have to be careful with the difference in the definition of the growth rate β. In their report, the growth rate with the present meaning was represented with a notation β_m. If the difference is taken into account, figure 8 of Larson & Wright (1975) can be converted into figure 13. The values of friction velocity for our results are represented by those measured at the fully developed stage, that is $u_{*a,st}$ listed in table 2, for the sake of ready comparison with their results. The crosses represent our results, where the wavenumbers are calculated from the frequency and the phase velocity of observed initial wavelets. The points with other symbols represent their results, and they are connected smoothly and somewhat arbitrarily by solid lines. The points with the maximum value of growth rate in each line are connected by a broken line. Since the line passes near the crosses, the consistency between the two experiments can be said to be confirmed. However, they are not necessarily consistent as to the dependence on $u_{*a,st}$. The inconsistency may be caused by differences of the wind-wave tunnels, the most important one being related to the presence or absence of a top cover.

3.3. *Properties of the mean velocity of air and water*

The velocity of the flow in the water was measured by a flow visualization technique described in § 2, from the start of the wind to the time when the technique becomes unusable due to halation and the distortion of hydrogen bubble lines by the wave

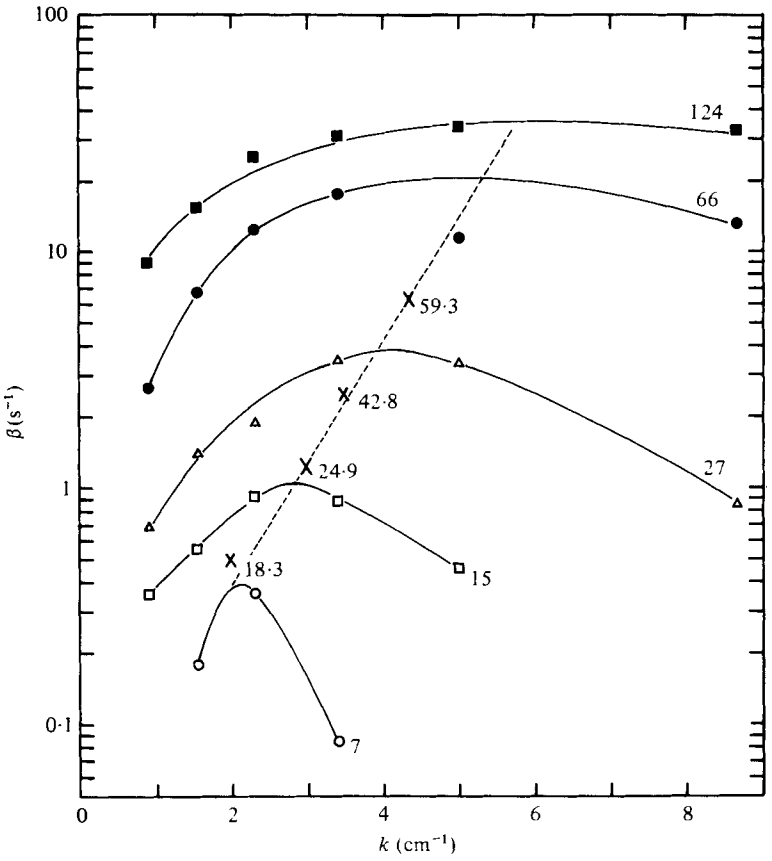

FIGURE 13. Correlation of growth rate β to wavenumber k. ■, ●, △, □, ○, converted from figure 8 of Larson & Wright (1975); ×, results of this study for the initial wavelets. Friction velocities in the air $u_{*a,st}$ measured at the fully developed stage are given in cm s^{-1}.

motion. Since the flow is laminar, the wind stress τ_0 exerted on the water surface can be estimated from the velocity gradient $U'_w(0)$ at the surface, through the relation

$$\tau_0 = \rho_w \nu_w U'_w(0), \tag{3.1}$$

where ρ_w and ν_w are the density and the molecular kinematic viscosity of the water, respectively. Kawai (1977*a*) has already shown that this estimation of the wind stress is accurate from comparison between the values thus estimated and those estimated from the wind profiles over the surface, where the wind waves are suppressed by addition of soap in the water, under the same wind conditions. The time series of the friction velocity $u_{*w} \equiv (\tau_0/\rho_w)^{\frac{1}{2}}$ of the water are shown in figure 14 for all cases of II. The counterparts of the figure for I are not shown because they have similar tendencies. The horizontal solid lines drawn in the figure represent the interval over which the initial wavelets are seen. The horizontal broken lines will be explained later in § 4. For each case of the experiment, the value of friction velocity approaches a constant value several seconds before the critical time of the first appearance of initial wavelets. The constant friction velocity lasts past the critical time until the observation ends due to the limitation of the technique. The constant values of the friction velocity

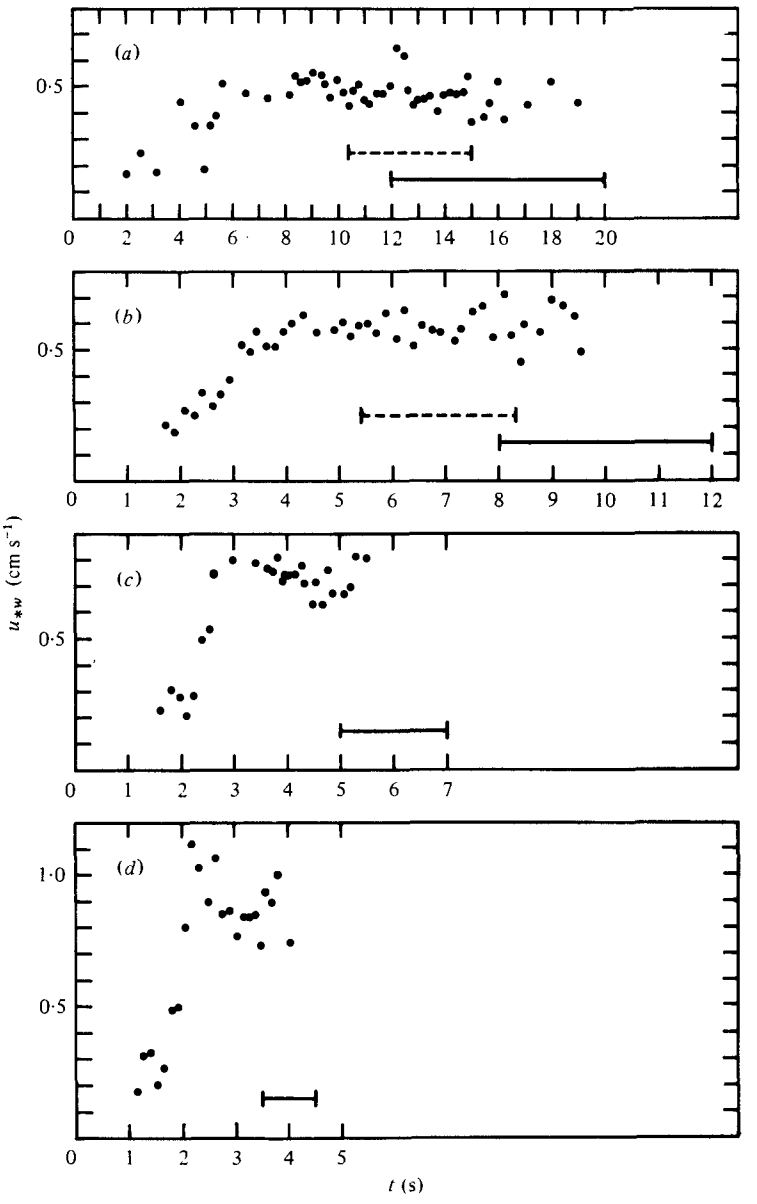

FIGURE 14. Time series of the friction velocity u_{*w} of the water, estimated from the observed velocity gradient in water at the interface for all cases of II. ——, the period in which the initial wavelets are seen; – – – – –, the period in which the observed velocity profiles in water can be well expressed with the functional form (4.16). (*a*) $U_r = 4{\cdot}2$ m s^{-1}; (*b*) $U_r = 5{\cdot}1$ m s^{-1}; (*c*) $U_r = 6{\cdot}3$ m s^{-1}; (*d*) $U_r = 7{\cdot}4$ m s^{-1}.

u_{*w} are listed in tables 1 and 2. The values u_{*a} in the tables are computed from the relation

$$\rho_a u_{*a}^2 = \rho_w u_{*w}^2, \tag{3.2}$$

where ρ_a is the density of the air, assuming the continuity of the shearing stress through the interface.

In figure 15 are shown the time series of the flow velocity U_0 at the interface. The significance of the inserted horizontal lines is the same as in figure 14. It should be noted that the rate of increase in U_0 becomes lower a few seconds after the critical time, as seen in the figure.

4. Formulation of the theory of shear flow instability

We consider a two-dimensional stationary laminar flow in the air and the water, which is parallel to the horizontal co-ordinate x with velocity profile $U = U(y)$, where the vertical co-ordinate y is taken positive upward from the still interface. The Orr–Sommerfeld equation is obtained from the first-order perturbation of the Navier–Stokes equation when the stationary flow is perturbed by a small disturbance whose stream function ψ has the form

$$\psi(x, y, t) = \phi(y) \exp[ik(x - ct)], \tag{4.1}$$

where k is a wavenumber and c is the complex wave velocity. Thus, the Orr–Sommerfeld equations are

$$(U_a - c)(\phi_a'' - k^2\phi_a) - U_a''\phi_a = (ikRe_a)^{-1}(\phi_a^{\mathrm{iv}} - 2k^2\phi_a'' + k^4\phi_a), \tag{4.2}$$

for the air motion and

$$(U_w - c)(\phi_w'' - k^2\phi_w) - U_w''\phi_w = (ikRe_w)^{-1}(\phi_w^{\mathrm{iv}} - 2k^2\phi_w'' + k^4\phi_w), \tag{4.3}$$

for the water motion, where Reynolds numbers are defined by the scale length δ, the scale velocity U_s and the molecular viscosity ν of fluids, as

$$Re_a = U_s\delta/\nu_a \quad \text{and} \quad Re_w = U_s\delta/\nu_w, \tag{4.4}$$

respectively, and where the variables with a subscript a or w stand for those in the air or in the water, respectively, the prime represents differentiation with respect to y, and all variables are normalized by the scale parameters.

At the interface the discontinuity in the normal stress must be balanced by the surface tension, and the shearing stress and the velocity components must be continuous. These boundary conditions and the kinematical boundary condition at the perturbed interface are expressed as Taylor series expansions about $y = 0$. If the higher-order terms in these series are neglected, some computations lead to four homogeneous boundary conditions in terms of ϕ in the expression (4.1), as follows,

$$\phi_a = \phi_w, \tag{4.5}$$

$$\frac{U_a'}{c - U_0}\phi_a + \phi_a' = \frac{U_w'}{c - U_0}\phi_w + \phi_w', \tag{4.6}$$

$$rs\left\{\left(\frac{U_a''}{c - U_0} + k^2\right)\phi_a + \phi_a''\right\} = \left(\frac{U_w''}{c - U_0} + k^2\right)\phi_w + \phi_w'', \tag{4.7}$$

$$s\left\{\left(U_a' - \frac{kc_0^2}{c - U_0}\right)\phi_a + (c - U_0 + 3ikRe_a^{-1})\phi_a' + \frac{\phi_a'''}{ikRe_a}\right\} = \left(U_w' - \frac{kc_0^2}{c - U_0}\right)\phi_w + (c - U_0 + 3ikRe_w^{-1})\phi_w' + \frac{\phi_w'''}{ikRe_w}, \tag{4.8}$$

respectively, at $y = 0$, where U_0 is the velocity of the basic flow at the interface, r the ratio of viscosity of the two fluids,

$$r = \nu_a/\nu_w, \tag{4.9}$$

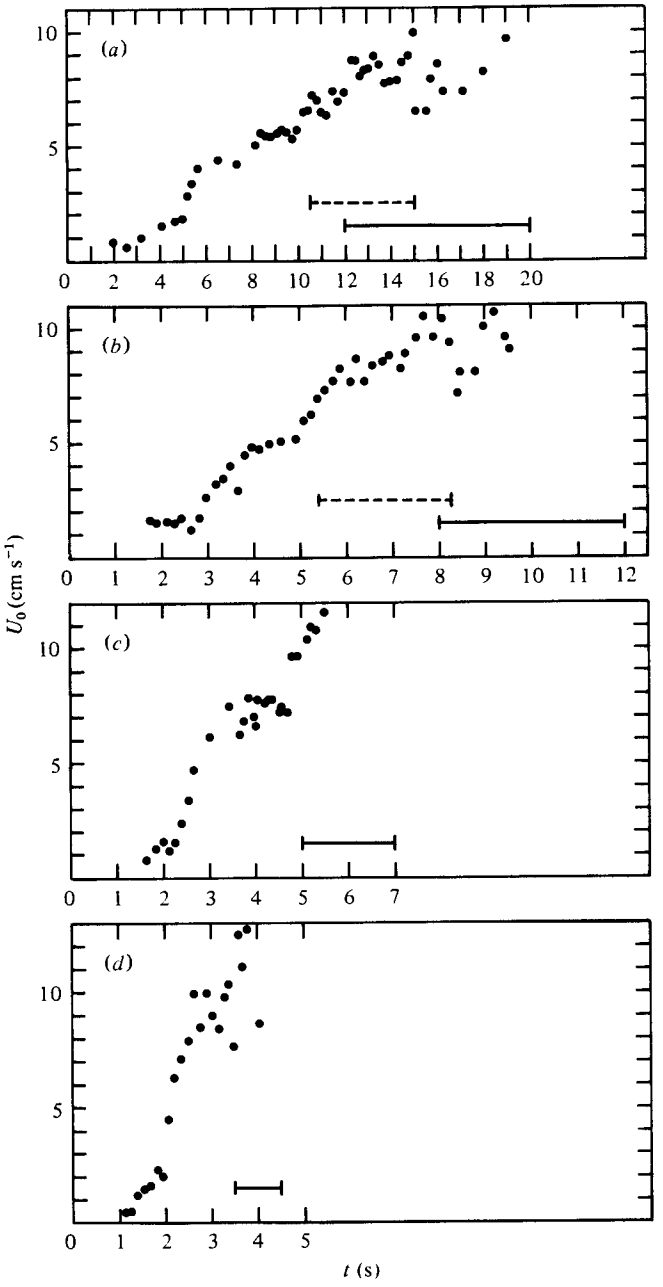

FIGURE 15. Time series of the observed velocity U_0 at the interface for all cases of II. The inserted horizontal lines have the same significance as in figure 14. (*a*) $U_r = 4{\cdot}2$ m s^{-1}; (*b*) $U_r = 5{\cdot}1$ m s^{-1}; (*c*) $U_r = 6{\cdot}3$ m s^{-1}; (*d*) $U_r = 7{\cdot}4$ m s^{-1}.

s is the ratio of the density of fluids

$$s = \rho_a/\rho_w \tag{4.10}$$

and c_0 is defined by

$$c_0^2 = (kFr)^{-1} + kWe^{-1}, \tag{4.11}$$

$$Fr = U_s^2/g\delta, \tag{4.12}$$

$$We = U_s^2\delta(\rho_w - \rho_a)/T, \tag{4.13}$$

where g is the acceleration due to gravity and T the surface tension. The boundary conditions at infinity are

$$\phi_a = \phi_a' = 0, \quad \text{at} \quad y = \infty, \tag{4.14}$$

$$\phi_w = \phi_w' = 0, \quad \text{at} \quad y = -\infty. \tag{4.15}$$

The basic equations formulated above are similar to those of Valenzuela (1976), but the pattern of the basic flow in the water is different. As the basic flow in the water, he assumed a steady logarithmic profile in the stability analysis. However, the observed basic flow in the water, at least up to the time when the initial wavelets appear, is neither steady nor logarithmic, as was described in the previous section. Moreover, since the difference of the basic flow in the water has a serious influence, through the difference of phase velocity, on the frequency of waves calculated from their wavenumber and phase velocity, the observed profiles are used for the basic flow in the water in the present study. To compare the observed properties of the initial wavelets with the properties expected from the theory of shear flow instability, computations are made mainly for the basic flow pattern measured at the critical time when the initial wavelets are observed for the first time in the experiment, and the results are compared with the values observed at the critical time.

To describe the observed velocity profile in the water with a functional form, the following expression is used:

$$U(y) = U_0[\exp(-\xi^2) + \pi^{\frac{1}{2}}\xi\{1 + \Phi(\xi)\}], \quad \text{for} \quad y \leqslant 0, \tag{4.16}$$

where U_0 is the surface velocity and expressed by

$$U_0 = 2\pi^{-\frac{1}{2}}u_{*w}^2\left(\frac{t - t_s}{\nu_w}\right)^{\frac{1}{2}}, \tag{4.17}$$

ξ is the dimensionless vertical co-ordinate and is expressed by

$$\xi = y/[2\{\nu_w(t - t_s)\}^{\frac{1}{2}}], \tag{4.18}$$

Φ is the error function defined by

$$\Phi(\xi) = 2\pi^{-\frac{1}{2}}\int_0^{\xi}\exp(-x^2)\,dx \tag{4.19}$$

and where t is the time from the start of the wind, and t_s a parameter which is decided from the condition that the formula fits best to the observed data. This functional form with $t_s = 0$ was originally introduced analytically by Kunishi (1957) for the laminar shear flow in the water produced by a constant wind stress at the interface. In the real conditions in the experiment, the stress was not constant at first but became constant a few seconds after the start of the wind, as shown in figure 14. However, if the parameter t_s for the effective shifting time of wind start is introduced, the flow

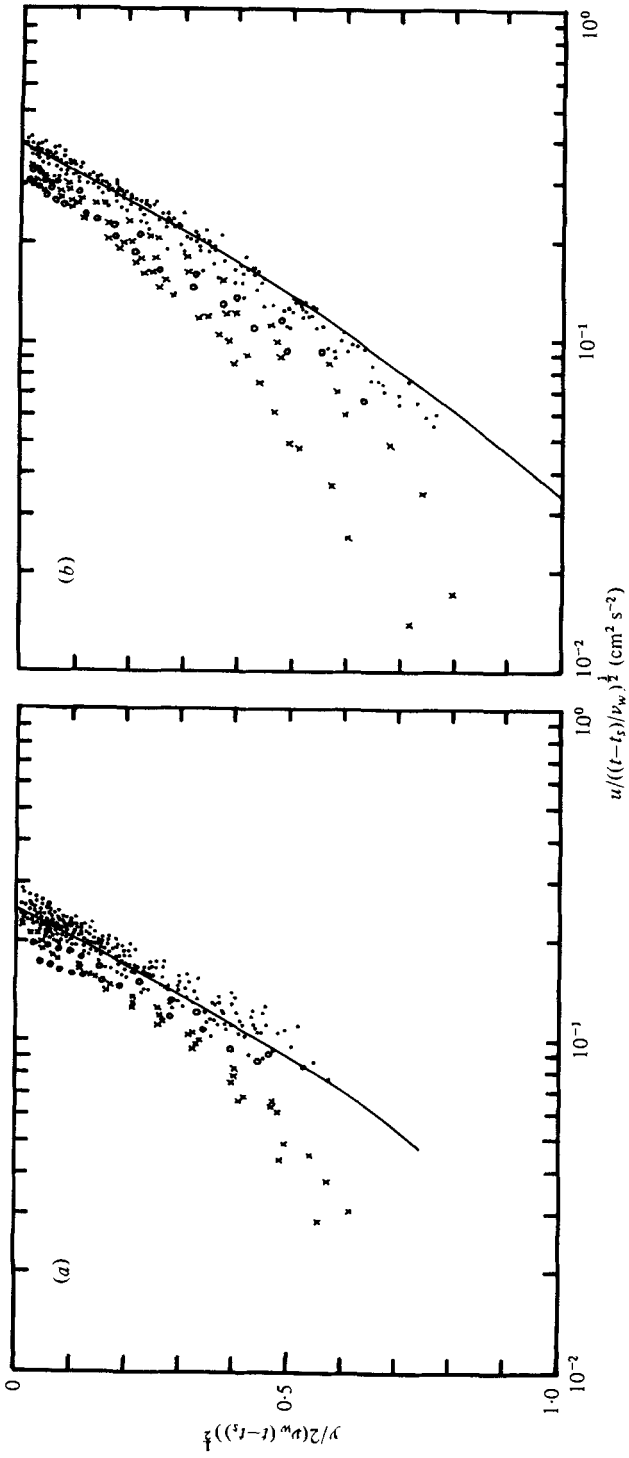

FIGURE 16. Normalized velocity profiles in water. Solid lines represent equation (4.16). Solid circles represent the observed data which are sampled from the interval when the observed data fit to (4.16) with adequate values of t_s: (*a*) $U_r = 4{\cdot}3$ m s^{-1}, $t_s = 3{\cdot}30$ s; (*b*) $U_r = 5{\cdot}5$ m s^{-1}, $t_s = 2{\cdot}15$ s. Ranges for t (s) are for (*a*): ×, 9·1–10·0; •, 10·5–15·0; ○, 15·6–16·3; ——, $u_{*w} = 0{\cdot}47$ cm s^{-1}; and for (*b*): ×, 4·0–5·2; •, 5·4–8·3; ○, 9·0–9·6; ——, $u_{*w} = 0{\cdot}59$ cm s^{-1}.

U_r (m s^{-1})	$5\nu_a/u_{*a}$ (cm)	$8\nu_a/u_{*a}$ (cm)
4·2	0·055	0·088
5·1	0·044	0·071
6·3	0·035	0·056
7·4	0·030	0·048

TABLE 3. Estimates of the thickness of viscous sublayer in air estimated from the observed value u_{*a} at the time of observation of the initial wavelets, for all cases of II.

pattern (4.16) agrees fairly well with the observed values for a certain time interval in the vicinity of the critical time when the initial wavelets are observed for the first time, for the cases of the lower two wind speeds. The agreement is tested in figure 16, where the normalized profiles observed in the interval are shown by solid circles and the equation (4.16) by solid lines. The intervals are shown in figure 14 and 15 by broken horizontal lines. For the cases of the higher two wind speeds, the observed velocity profiles in the water do not necessarily follow the functional form (4.16) in the vicinity of the critical time when the initial wavelets are first observed, presumably because the critical time is so close to the time of the attainment of constant wind stress; therefore the water flow driven by the increasing wind stress occupies a non-negligible part of the water flow even at the critical time. Nevertheless, the functional form is used also for these cases under the condition that the observed surface velocity U_0 coincides with the functional value. The influence of the difference in the flow pattern in the water will be examined in § 6.

In contrast with these circumstances in the water, we have no observation of the shear flow pattern in the air except that in the state where wind waves are fully developed, and the structure of the air flow must be different from that at the critical time when the initial wavelets are first observed. For the latter state, however, the air flow is expected to be aerodynamically smooth, since the wave height at the critical time is 0·0025 to 0·005 cm and far smaller than the thickness of the viscous sublayer in any case as shown in table 3, although wind waves cannot be simply regarded as roughness elements when the wave height is larger than the thickness of the viscous sublayer. As the smooth flow pattern, a modified form of the pattern proposed and verified with observed data by Miles (1957*b*) is used, in which the wind speed U at the height y is represented by

$$U(y) = (u_{*a}^2/\nu_a)\, y + U_0 \quad \text{for} \quad 0 \leqslant y \leqslant y_1 \tag{4.20}$$

in the viscous sublayer and by

$$U(y) = U_1 + (u_{*a}/\kappa)\,(\alpha - \tanh \tfrac{1}{2}\alpha) + U_0 \quad \text{for} \quad y_1 \leqslant y, \tag{4.21}$$

outside the sublayer. In this latter expression, α satisfies

$$\sinh \alpha = (2\kappa u_{*a}/\nu_a)\,(y - y_1), \tag{4.22}$$

where κ is von Kármán's constant with a constant value of 0·4, y_1 the thickness of the viscous sublayer, $U_1 + U_0$ the velocity at $y = y_1$ and U_0 the observed surface velocity. According to Monin & Yaglom (1971) the dimensionless sublayer thickness

U_r (m s^{-1})	$1/2(t-t_s)$ (s^{-1})	β (s^{-1})	ω (s^{-1})
4·2	0·06	0·5	66
5·1	0·09	1·3	91
6·3	0·2	2·5	107
7·4	0·3	6·3	129

TABLE 4. Comparison among the changing rate of observed basic flow, the observed growth rate and the observed angular frequency of initial wavelets, for all cases of II.

$y_1 u_{*a}/\nu_a$ which is equal to U_1/u_{*a}, is 5·0 for the smooth flow. However, from the necessity that (4.21) coincides with the logarithmic law,

$$U(y) = \frac{u_{*a}}{\kappa} \ln \frac{y u_{*a}}{\nu_a} + B u_{*a} + U_0, \tag{4.23}$$

at heights far above the sublayer, there is a relation between U_1/u_{*a} and B,

$$U_1/u_{*a} = B + 1{\cdot}3. \tag{4.24}$$

If the most usual value 5·5 is taken for B, U_1/u_{*a} is 6·8. Considering these circumstances and the slight indefiniteness of B mentioned by Monin & Yaglom (1971), computations are made for the two values of U_1/u_{*a} of 5·0 and 8·0.

Not only the basic shear flow in the water is time dependent, as seen from (4.17) and (4.18), but also that in the air is time dependent through U_0 in (4.20) and (4.21). In the present study, computations are made under the hypothetical condition of quasi-steady state for the basic flow. For the hypothetical condition to be applied, the rate of change of the basic flow $(\partial U/\partial t)/U$ must be much smaller than the angular frequency ω of initial wavelets. In this context, it is worthwhile to note that the growth rate β of the wave energy must be much smaller than ω, for the spectra calculated in the foregoing section under the same hypothetical condition to be meaningful. If the equation (4.17) which has the greatest rate of change in time is taken as the characteristic value of the basic flow, the rate of change of the basic flow is $1/2(t-t_s)$. With the observed values of ω, β and t which is taken as the critical time when the initial wavelets are observed for the first time, the two conditions are fulfilled, as shown in table 4.

5. Numerical procedures of the problem

The stability of the shear flow in both fluids, air and water, has been analysed by a number of investigators. Lock (1954) analysed the stability of the flow in the laminar boundary layer between parallel streams in the air and water. However, the results cannot be applied to the present problem, since the basic flow pattern in the analysis was very different from that observed in the present experiments. Miles (1962) analysed the stability of the logarithmic shear flow pattern of the air flows when the wave motion in the water was taken into account, but he neglected the basic flow in the water. Since the basic flow pattern in the water has a great influence on the phase velocity of waves, especially on that of short waves which are investigated in the present study, we cannot neglect the basic flow in the water. Larnaes (1976) also pointed out

that the basic flow in the water plays an important role in deciding the characteristics of waves generated by the instability mechanism. Although Shemdin (1972) discussed the influence of the shear flow in both fluids, on the characteristics of surface waves, his results also cannot be applied to the present problem, since he did not take into account the viscosity of fluids and treated only stationary waves.

The exact analysis of the shear flow instability mechanism for the two-layer viscous fluids of the air and the water was first made by Valenzuela (1976). In the analysis, he examined the correlation of the growth rate of waves with the friction velocity of the air for six wavenumbers which correspond to the cases of Larson & Wright (1975) experiment, in which only the initial growth rate of waves was measured. In contrast with them, we measured the frequency, the growth rate and the phase velocity of the initial wavelets, and our problem is whether or not the observed properties of the initial wavelets coincide with the properties of the waves whose growth rate, as predicted by the instability theory applied to the present model, is a maximum. To solve the problem, the correlation between the growth rate of waves and the wave number is examined when the basic flow is fixed. The correlation first gives the wavenumber of waves whose growth rate is maximum, and then the values of frequency, growth rate and phase velocity of the waves can be obtained from the correlation of these properties with wavenumber.

The problem formulated in the previous section is an eigenvalue problem, in which an eigenvalue c has to be decided under the given wavenumber k, the basic flow pattern designated by $U_a(y)$, $U''_a(y)$, $U'_a(0)$, $U_w(y)$, $U''_w(y)$ and $U'_w(0)$, the physical properties of fluids ρ_a, ρ_w, ν_a, ν_w and T and the acceleration due to gravity g. The problem is solved using the following procedures. First, two independent particular solutions satisfying the boundary conditions at infinity are solved in the air, and two in the water, with direct integration of the Orr–Sommerfeld equation by use of a Runge–Kutta numerical method, under a trial eigenvalue c. Then the error in the trial eigenvalue is estimated by examining how well those particular solutions satisfy the boundary conditions at the interface. With the estimated error, the trial eigenvalue is corrected and a new trial eigenvalue is examined in the same way. The iteration is continued until one is found to the desired accuracy.

These procedures are similar to those shown in § 14 of the monograph by Betchov & Criminale (1967), except for the following three slight changes. The first is in the way of purifying the numerical solutions. Although several methods are demonstrated in the monograph, we adopted another method which is shown in appendix A of this article, since the latter is easier for us to understand. In the appendix, a brief explanation is also given why the numerical solutions have to be purified in the course of numerical integration. The purification was performed at every fifth step of the numerical integration, and it is shown that the eigenvalue determined under the condition is not different from that with the purification at every step.

The second change is in the formula to estimate the error in the trial eigenvalue. This change is based on the difference of the region to be analysed. The formula used in this article is shown in appendix B, although the change is not essential.

The third change is in the numerical treatment of the boundary conditions at infinity. Since the basic flow velocity (4.21) in the air increases infinitely with an increase of y, we cannot apply such a technique as applied in the monograph to the problem of the Blasius-type flow whose velocity approaches a constant value

asymptotically. To overcome this problem, the basic flow pattern in the air outside the region of numerical integration is assumed as follows:

$$U(y) = U(y_{sa}),\ U''(y) = U''(y_{sa}) \quad \text{for} \quad y_{sa} \leqslant y, \tag{5.1}$$

where y_{sa} represents the edge of the region. Moreover, for consistency with the present procedures of the numerical integration, the continuity of U' has to be assumed at $y = y_{sa}$. With these assumptions, analytical particular solutions are given ouside the region of numerical integration, and they are used to specify the boundary conditions at $y = y_{sa}$. Although consideration easily shows that such a pattern cannot exist in any sense, the unreality of the pattern has no influence on the computational result, if y_{sa} is sufficiently large. These effects are caused by the nature of the surface waves whose influence decreases exponentially with height. In the case of the two-layer model now considered, this technique is applied also to the solution in the water. The values of y_{sa} and its counterpart in the water y_{sw} are decided from the condition that the eigenvalue determined from certain values of y_{sa} and y_{sw} attains the same value, with the desired accuracy, as that determined from twice their values. In most cases of our computation, the value of half the wavelength of the wave considered is sufficient.

The value of the interval h of the numerical integration or the number N_s of steps of the integration is decided from the condition that the eigenvalue determined under a certain value of h attains the same value, with the desired accuracy, with that determined using half its value. For the integration in the water h is set to be constant, and $N_s = 300$ is sufficient in most cases. For the integration in the air, however, a very large number of steps is necessary if h is taken as constant, because the required accuracy in the integration in the neighbourhood of the critical layer, which exists at a relatively lower position in the region of integration, demands small values of h. To overcome this problem, h is changed at the point whose height is from 3 to 30 times the height of the critical layer. Below the critical layer, 10 to 40 steps are taken for the integration. The total number N_s of 500 in the air is sufficient in most cases.

The problem was solved with an accuracy of 10^{-6} in terms of the relative error, since the value of the imaginary part of an eigenvalue c_i must be decided with an accuracy of 10^{-4} cm s^{-1} to decide accurately the wavenumber k whose kc_i is maximum, and the magnitude of c_r is of order 30 cm s^{-1}.

6. Results of numerical computation and comparison with observed properties

The numerical computations were made for four patterns of basic flow corresponding to the cases of experiment II. The values of physical properties of the two fluids used in the computation are $\rho_a = 1{\cdot}2 \times 10^{-3}$, $\rho_w = 1{\cdot}0$, $\nu_a = 0{\cdot}15$, $\nu_w = 0{\cdot}01$ and $T = 72{\cdot}5$, where all values are in c.g.s. units, and correspond to the observed values. Figure 17 shows the correlation of the frequency f, the growth rate kc_i and the phase velocity c_r with the wavenumber k, for the case $U_1/u_{*a} = 5{\cdot}0$. In the figure, U_0 is the velocity at the interface used in the computation, which is equal to the observed value at the critical time when the initial wavelets were observed for the first time. Similar figures can be drawn for the case $U_1/u_{*a} = 8{\cdot}0$. For any wind speed, there exists a wavenumber where kc_i is maximum, and the wavenumber does not necessarily coincide with the wavenumber of waves whose phase velocity is minimum, although the former is in the vicinity of the latter. This fact shows that it is risky to discuss the

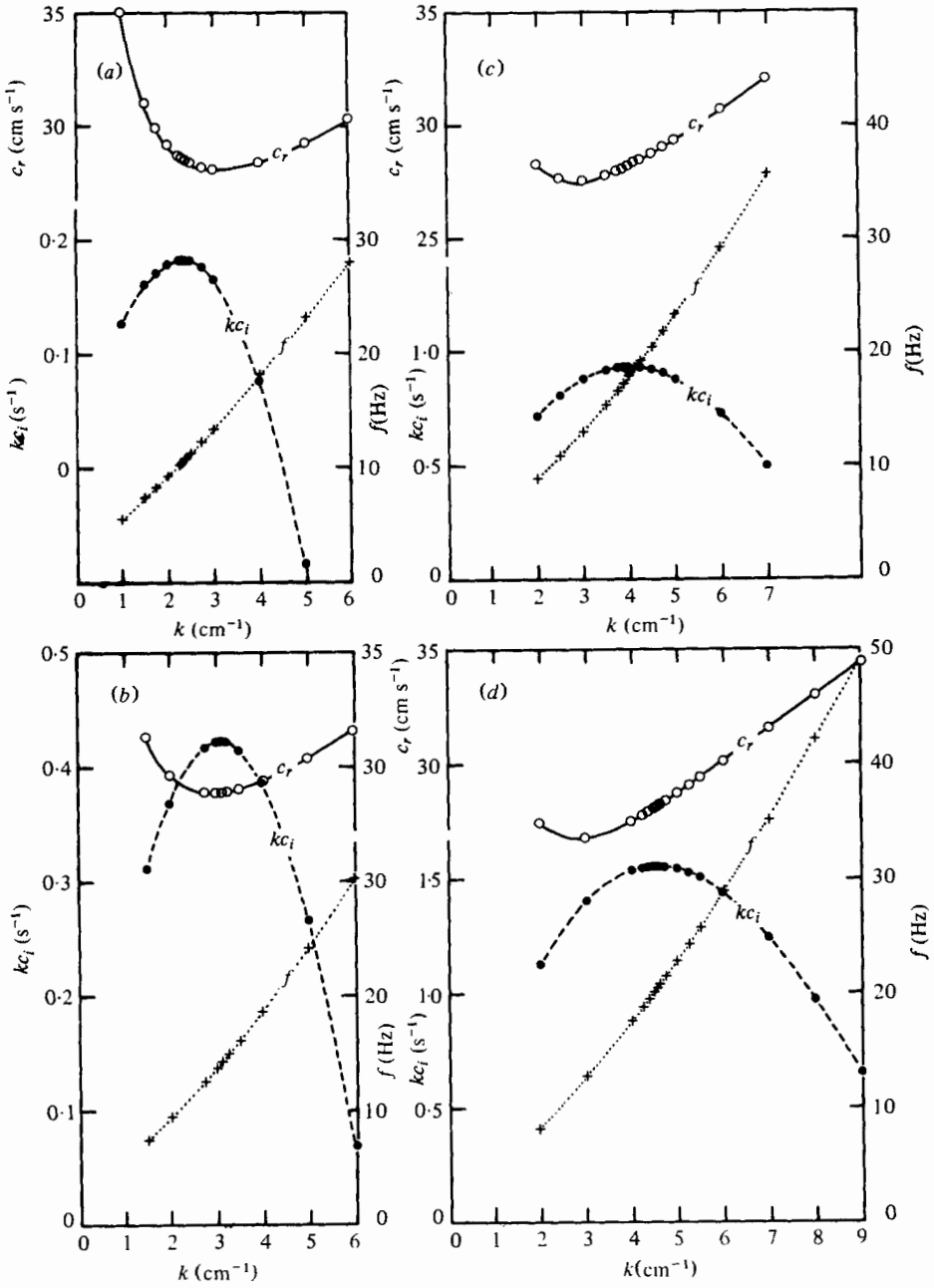

FIGURE 17. Correlation of the growth rate kc_i, the phase velocity c_r and the frequency f to the wavenumber k, computed with the two-layer model for the cases corresponding to those of II and $U_1/u_{*a} = 5{\cdot}0$. U_0 is the velocity at the interface used in the computation and equal to the observed value at the critical time of the first appearance of the initial wavelets. (*a*) $u_{*a} = 13{\cdot}6$ cm s^{-1}, $U_0 = 7{\cdot}5$ cm s^{-1}. (*b*) $u_{*a} = 17{\cdot}0$ cm s^{-1}, $U_0 = 9{\cdot}6$ cm s^{-1}. (*c*) $u_{*a} = 21{\cdot}4$ cm s^{-1}, $U_0 = 9{\cdot}8$ cm s^{-1}. (*d*) $u_{*a} = 24{\cdot}8$ cm s^{-1}, $U_0 = 10{\cdot}2$ cm s^{-1}.

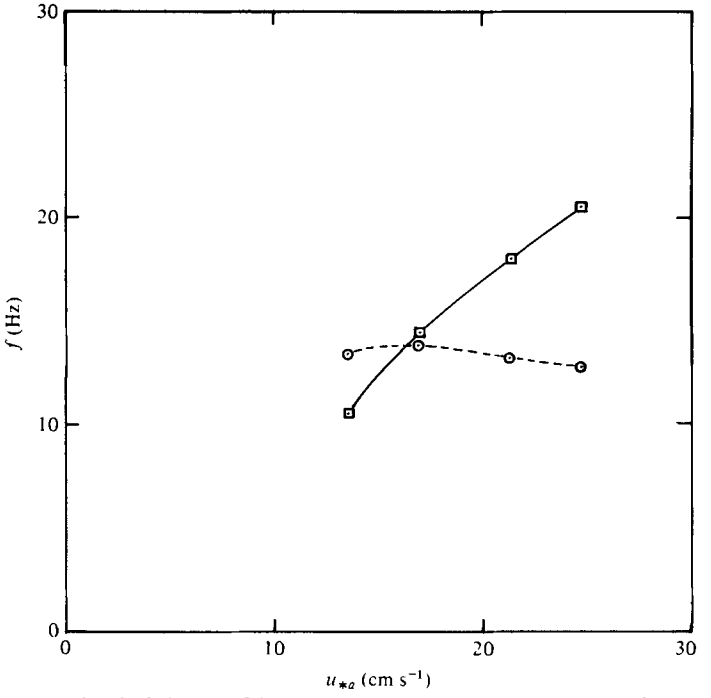

FIGURE 18. Frequencies f of the two kinds of critical waves, computed with the two-layer model, as a function of u_{*a} for the case $U_1/u_{*a} = 5{\cdot}0$. ⊡, kc_i is a maximum; ⊙, c_r is a minimum.

mechanism relating to a phenomenon from its single aspect, since we might conclude that the initial wavelets are the waves whose phase velocity is minimum, if we did not know any other properties than the phase velocity of initial wavelets. Fortunately, we now have three aspects for the examination of the observed phenomena: the frequency, the growth rate and the phase velocity. The above two kinds of critical waves can clearly be discriminated in figure 18 where their frequencies are plotted as a function of u_{*a}, for the case $U_1/u_{*a} = 5{\cdot}0$.

Figure 8 shows, together with the frequency of the initial wavelets observed in our experiment described in § 3, the calculated values of frequency f_i of the waves whose kc_i is maximum, as a function of u_{*a}. Squares are used for the case $U_1/u_{*a} = 5{\cdot}0$ and triangles for the case $U_1/u_{*a} = 8{\cdot}0$, and the points are connected smoothly by broken lines. There is no significant difference between the lines of calculated values and the points of observed data. Consequently, it is concluded that the observed frequency of the initial wavelets coincides with the frequency of the waves whose growth rate expected by the shear flow instability theory is maximum. The fact shown in figure 18, together with figure 8, emphasizes the inefficacy of Phillips' (1957) resonance mechanism as the generation mechanism of initial wavelets, although the inefficacy has been already suggested by the discrepancy in the type of growth in time.

It is worthwhile to note here our speculation on the cause of the difference between the frequencies of the temporal and spatial initial wavelets which can be clearly seen in figure 8. Plate *et al.* (1969) who measured the spatial initial wavelets, transformed the temporal growth rate β_t computed by Miles (1962) into the spatial growth rate β_x through the relation

$$\beta_x = \beta_t / c_g, \tag{6.1}$$

where c_g is the group velocity, but they did not take into account the influence of the relation on the frequency of the waves whose spatial growth rate is maximum. If the relation (6.1) is accepted, the frequency of the waves whose spatial growth rate is maximum does not necessarily coincide with the frequency of the waves whose temporal growth rate is maximum, since the group velocity is dependent in general on the wavenumber. In fact, some estimations from the results shown in figure 17, through the relation (6.1) together with

$$c_g = c_r + k\,\partial c_r/\partial k, \tag{6.2}$$

where the derivative is approximated by the corresponding finite difference, show the lowering of the frequency for the waves whose spatial growth rate is a maximum from that for temporal ones. Although the sense of the difference between the two kinds of critical frequency is useful to explain the difference between the observed frequencies of the two kinds of initial wavelets, we cannot draw definite conclusions, since the step in k in the above results shown in figure 17 is too coarse to estimate accurately the derivative in (6.2), except for the neighbourhood of the waves whose temporal growth rate is maximum. The difference between the two kinds of frequency may not be cancelled by only the transformation (6.1), since the transformation is an approximate relation which is correct only in the case of near-neutral conditions, as was shown by Gaster (1962). Essentially, the spatial growth rate of the spatial initial wavelets, has to be discussed in relation to the model in which the perturbation has a complex wave-number and a real frequency, instead of the present model in which the perturbation has a real wavenumber and a complex frequency. The examination of the former model and the precise verification of the relation (6.1) are future problems.

Figure 9 shows, together with the energy growth rate of the initial wavelets observed in our experiment described in § 3, the calculated values of energy growth rate β or $2kc_i$ of the waves whose kc_i is maximum, as a function of u_{*a}, with the same symbols as in figure 8. If an emphasis is placed on the values from II that are more reliable than those from I, the observed values fall between the two computational cases $U_1/u_{*a} = 5{\cdot}0$ and $8{\cdot}0$, with an exception for the case of the highest wind speed. Moreover, the points of I do not deviate so far from the lines of computation. In the case of the highest wind speed, since the duration of the initial wavelets was so short that the energy growth rate was computed from only two spectra, the observed value has poor accuracy. As a result, we can also conclude that the observed growth rate of the initial wavelets coincides with the maximum growth rate expected by the shear flow instability theory.

Figure 19 shows the computed phase velocity c_r of the waves whose kc_i is maximum, together with the observed phase velocity of the initial wavelets, as a function of u_{*a}. The observed values for the cases of the highest three wind speeds were determined at the critical time when the initial wavelets were observed for the first time. For the case of the lowest wind speed, the phase velocity at the critical time could not be observed because of a limitation of the technique, and the value plotted in the figure is that observed about 3·5 s later. Therefore the value for the case is presumably a little larger relatively, as expected from the trend of U_0 in figure 15 (a). Even if these circumstances are taken into account, the observed values are slightly larger than the computed values.

Although the slight disagreement in the phase velocity is not yet explained, it can

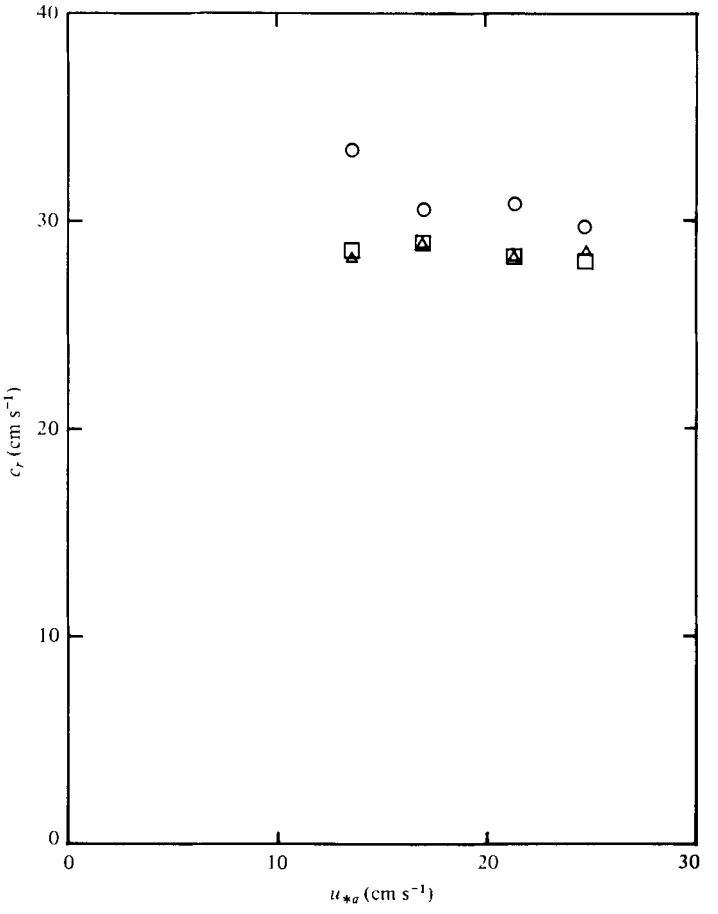

FIGURE 19. Correlation between u_{*a} and the phase velocity c_r of the observed initial wavelets together with c_r of the waves whose theoretical growth rate is maximum. The observed values for the cases of the higher three wind speeds are observed at the critical time of the first appearance of the initial wavelets. The observed value for the case of the lowest wind speed is obtained at about 3·5 s after the critical time, because of the experimental difficulties stated in the text. ○, experiment II; □, theory, $U_1/u_{*a} = 5{\cdot}0$; △, theory, $U_1/u_{*a} = 8{\cdot}0$.

be concluded that the initial wavelets are the waves generated by the instability mechanism taking into account the shear flow in the air and water, since the three properties of the initial wavelets coincide fairly well with those of the waves whose growth rate expected by the shear flow instability theory is maximum.

To examine the influence of the time dependent basic flow in the water, figure 20 shows the contours of kc_i in the Re, k plane, from the state of no flow in the water to the state at the time when the initial wavelets were first observed, for the case $U_r = 4{\cdot}2$ m s^{-1} and $U_1/u_{*a} = 5{\cdot}0$. In the figure the Reynolds number Re is defined by

$$Re = U_0 \delta / \nu_w, \tag{6.3}$$

where U_0 is the surface velocity defined by (4.17) and δ is the scale thickness of the surface boundary layer in the water defined by

$$\delta = 2[\nu_w(t - t_s)]^{\frac{1}{2}}. \tag{6.4}$$

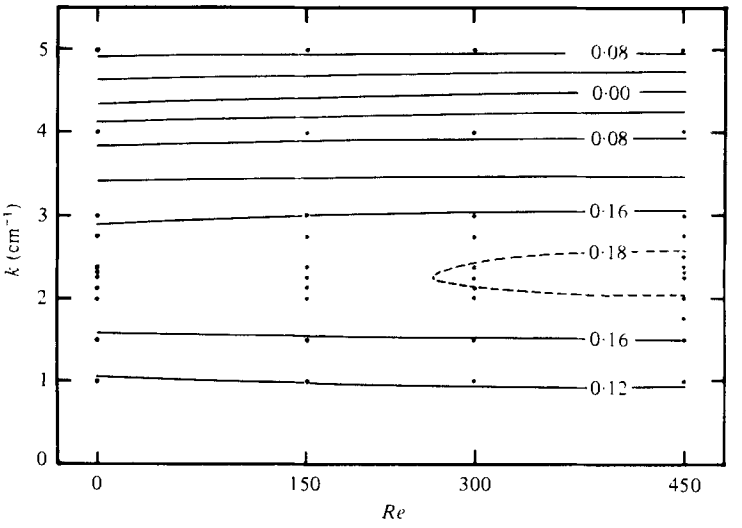

FIGURE 20. Contours of kc_i in Re, k plane computed with the two-layer model for the case $U_r = 4{\cdot}2$ m s^{-1} and $U_1/u_{*a} = 5{\cdot}0$. Reynolds number Re in this figure is a linear function of time and expressed by (6.5). Solid circles represent the computed points.

As seen from these definitions, Reynolds number so defined is a linear function of the time and expressed by

$$Re = 4\pi^{-\frac{1}{2}} u_{*w}^2 (t - t_s)/\nu_w, \tag{6.5}$$

where u_{*w} is the constant friction velocity of the water listed in table 2. In the figure the wavenumber k of the waves whose kc_i is maximum, scarcely changes with time. If attention is paid to the waves whose kc_i is maximum, their phase velocity increases with time due to the increase of the advective velocity in the water, therefore their frequency also increases with time. From this fact, it might be better to measure the growth of the wavenumber spectrum than to measure the frequency spectrum, in order to grasp the phenomena of initial wavelet generation. However, we have not succeeded in measuring them up to the present. Although Larson & Wright (1975) measured the energy growth rate of waves whose wavenumber is fixed, as already mentioned in § 1, they were also unable to obtain the continuous spectrum of waves.

In spite of the possible dependence on time of the frequency of the waves whose kc_i is maximum, the present experiment showed that there exist initial wavelets whose frequency is almost constant in time. This result is presumably due to the fact that the duration in which the initial wavelets can be detected was relatively short, and that the basic flow pattern did not develop constantly following (4.16) but changed to the pattern whose surface velocity is nearly constant in time, as seen in figure 15, a short time after the critical time when the initial wavelets were first observed.

Finally, we have to examine the problem that the basic flow pattern in the water expressed by (4.16) did not necessarily correspond to the observed pattern, for the cases of the two higher wind speeds. The observed patterns fell between the pattern (4.16) and a linear pattern, as expected from the accelerated tendency of u_{*w} shown in figure 14. As another limit of the basic flow pattern in the water, computations

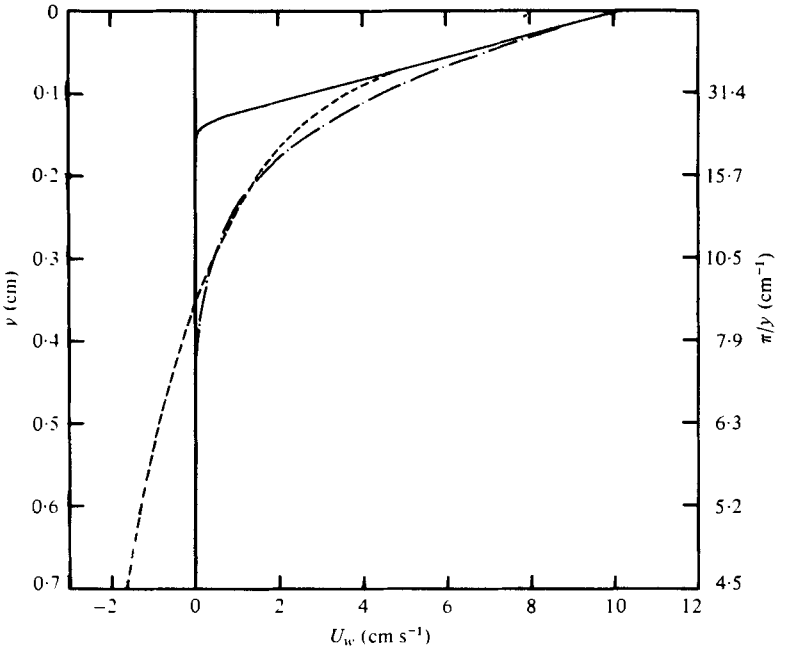

FIGURE 21. Three types of shear flow pattern in the water for the case of $u_{*a} = 24{\cdot}8$ cm s^{-1} and $U_0 = 10{\cdot}2$ cm s^{-1}. ——, (6.6); — · —, (4.16); – – – – –, logarithmic profile used by Valenzuela (1976) with $U_1/u_* = 5{\cdot}0$ and $U_0 = 10{\cdot}2$ cm s^{-1}. π/y is the wavenumber of waves whose wavelength is $2y$.

were made for the cases of the higher two wind speeds with the linear pattern where the velocity decreases linearly downward from the observed surface velocity U_0 to zero, and in the deeper portion it is uniformly zero. As this pattern, however, has a discontinuous point of velocity gradient and cannot be treated by the two-layer model, a pattern which resembles this was used in which there is no discontinuous point of U, U' and U'', as follows:

$$\left.\begin{aligned} U(y) &= U_0(1-y/y_0) \quad \text{for} \quad 0 \geqslant y \geqslant ly_0, \\ U(y) &= U_0(1-l)\left\{1-\tanh\left(\frac{(y/y_0)-l}{1-l}\right)\right\} \quad \text{for} \quad y \leqslant ly_0, \end{aligned}\right\} \tag{6.6}$$

where $|y_0|$ is the depth where U' has a discontinuity in the original pattern. This is related to u_{*w} by

$$u_{*w}^2 = \nu_w U_0/|y_0|, \tag{6.7}$$

and l is set to 0·9. Since the differences between the computational result with the pattern (6.6) and that with (4.16) are smaller than 1 Hz in frequency f, 10 % in the growth rate kc_i and 1 cm s^{-1} in the phase velocity c_r, for the waves whose kc_i is maximum, the above conclusion is not changed.

Since the examination in the foregoing paragraph shows that the shear flow pattern in the water has rather little effect on the eigenvalue, we should discuss further the logarithmic profile in the water used by Valenzuela (1976). The three patterns relating to the present discussion are shown in figure 21 for the case $u_{*a} = 24{\cdot}8$ cm s^{-1} and

$U_0 = 10{\cdot}2$ cm s^{-1}. The logarithmic pattern in the figure is drawn following the definition by Valenzuela (1976) with parameters $U_1/u_* = 5{\cdot}0$ and $U_0 = 10{\cdot}2$ cm s^{-1}. The scale of the abscissa shown on the right-hand side of the figure represents the wavenumber of waves whose wavelength is twice the depth at the point. In the shallower region where the flow pattern has greater influence on the eigenvalue, the logarithmic pattern falls between (4.16) and (6.6), and one can expect that the eigenvalue obtained with the logarithmic pattern is only slightly different from the present results. In fact, the growth rates calculated by Valenzuela (1976) are near the present results, if the difference in his definition of the growth rate from ours is taken into account. However, as to the other properties of the eigenvalue, significant difference exists owing to the difference in U_0. If we use the relation

$$U_0 = \frac{0{\cdot}04}{0{\cdot}05} u_{*a}, \tag{6.8}$$

to decide U_0, which was used by Valenzuela (1976), U_0 is 19·8 cm s^{-1} for this case and far greater than the observed value. This difference has a direct influence on the phase velocity and the frequency, although not on the growth rate.

7. Discussion and conclusion

We have to discuss first the reason why the initial wavelets could not be measured until several seconds after the start of the wind in the present experiments. The wave heights of the initial wavelets at the critical time of their first appearance ranged from 0·025 to 0·05 mm. On the other hand, the minimum value detectable by the wave gauge was less than or equal to 0·0262 mm, as shown in figure 5. This might be the cause, because the minimum wave heights measured were near to this value.

By using instruments with higher resolving power, Larson & Wright (1975) also observed the temporal growth process of wind waves and reported that the exponential growth started at the same time as the wind started. Their results support the inference that the insufficient resolving power of our instrument is the cause of the disappearance of initial wavelets for the initial few seconds in our records. Although Plant & Wright (1977) reported, by use of the same instruments as those of Larson & Wright, that the exponential growth started several seconds to a few tens of seconds later than the wind, their results should not be interpreted as denying the present inference, since the wavenumber range measured by Plant & Wright did not cover the initial wavelets. On the other hand, the experiment of Larson & Wright did cover them, as shown in figure 13.

If the above discussion is taken into account, it is concluded from the results obtained in this paper, that the generation and growth processes of initial wavelets are controlled by the instability mechanism entirely, from the time at which the wind starts to the time at which they reach their maximum heights.

In contrast to this conclusion, the instability mechanism has so far been considered efficient as the growth mechanism of wind waves, and not as their generation mechanism. As the generation mechanism, Phillips' (1957) resonance mechanism has been thought to be efficient, since Miles (1960) proposed the Phillips–Miles combined mechanism. This point of view was based on the fact that the instability mechanism is not efficient unless some initial waves, no matter how small they are, pre-exist due

to some generation mechanism. It has been shown in the present study, however, that the initial wavelets are the waves whose growth rate by the instability mechanism is maximum, or, in other words, they are the waves selected by the instability mechanism. More precisely, the generation of wind waves whose initial stage is called the initial wavelets is caused by the selective amplification of 'the small perturbations which inevitably occur in the flow', by the instability mechanism. The phrase quoted is from the section 'Turbulence' in Landau & Lifshitz (1959), and, with a similar point of view, Schubauer & Skramstad (1947) explained the generation of the natural oscillatory motion (Tollmien–Schlichting waves) which appears in the boundary flow above flat plates.

Based on the classification by Benjamin (1963) and its interpretation by Turner (1973), there are three types of instability which can occur at a density interface across which there is a velocity difference. They are called class A instability which is related to Tollmien–Schlichting waves, class B instability which is related to free surface waves and class C or Kelvin–Helmholtz instability. The phase velocity of the perturbation waves calculated in the present analysis is near to that of free surface waves when the shear flow in the water is taken into account; consequently the instability relating to the initial wavelets might be interpreted as belonging to class B. However, it may not belong to class B, if the physical interpretation given to the class B instability by Benjamin and Turner is adopted. They stated that the essential factor for the class B instability is the curvature of the wind profile at the critical height where $U = c_r$, while, in all the cases of the present study, the critical height was in the viscous sublayer and the curvature at that height was zero. In this sense, the instability relating to the initial wavelets should be interpreted as representing a new type of instability or modified class B instability.

Finally, the limitation of the linear instability theory as applied to the growth process of wind waves should be discussed. So far we have focused the discussion on the initial wavelets or the waves which are long-crested, regular and which appear at the initial stage of the generation and growth processes of wind waves. However, the duration of the initial wavelets after the start of the wind is very short, and in our experiments it ranges from 5 s for $U_r = 7{\cdot}4$ m s^{-1} to 20 s for $U_r = 4{\cdot}2$ m s^{-1}, as seen for example in figure 14. After this short duration, the water surface becomes covered by short-crested and irregular waves. The change of the surface state is distinctly visible, as was shown in figure 1, and the time of the visual change of the surface corresponds to the time when the energy of the initial wavelets reaches its maximum value. After that time, the spectral peak starts to move toward the lower frequency as the energy is increased; the general trend is seen in figure 10. However, individual time series of the spectral peak show complicated movements, as seen in figure 7. On closer inspection, the complicated movements of the spectral peak can be seen also in the average spectra. Figure 22 shows a continuation of the time series of the movement of the spectral peak for the same case as that of figure 11 (b). Each point, shown in an alphabetical order according to the lapse of time, represents the peak of the averaged spectra for the case of $U_r = 5{\cdot}1$ m s^{-1}. The conditions of the data analysis are the same as in the case of initial wavelets shown in figure 11 (b). As a result, the sampling interval and the data length per sample for the developing stage of the wind waves are much shorter than those in figure 10. The points A through J correspond to the peaks of the initial-wavelet spectra shown in figure 11 (b). Further complicated movements of

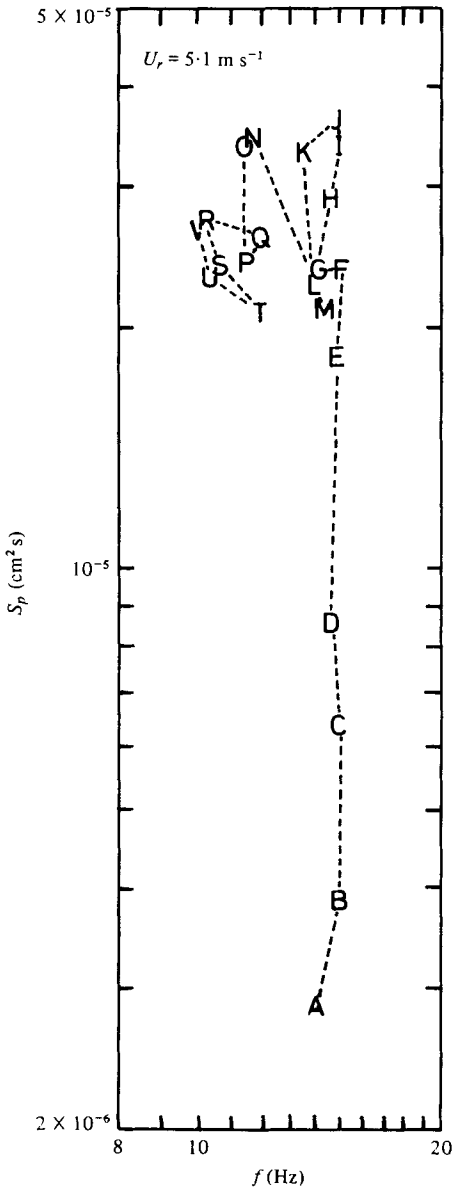

FIGURE 22. Detailed inspection of the observed time series of spectral peak for the case U_r = 5·1 m s^{-1} of II. The passage of time is indicated by alphabetical order. The interval between successive points is 0·32 s. Δt = 0·005 s, N = 128 and NS = 8. The equation $L = 2\sqrt{N}$ and FPE criterion are used.

the spectral peak may be interpreted as demonstrating that the linear instability theory cannot be applied to the stage after the duration of the initial wavelets, since the theory still expects a monotonic growth of waves.

On the other hand, we have been investigating, simultaneously with the present study, the structure of the fetch-limited wind waves mainly by use of flow visualization techniques (Toba *et al.* 1975; Okuda *et al.* 1976; Okuda *et al.* 1977). From these studies,

it was shown that the wind waves are accompanied by some systematic or organized forced convection relative to the individual crests, and consequently that an expression in terms of linear equations is impossible. In this sense, those statistically stationary but irregular wind waves and the initial wavelets are quite different phenomena from each other. We cannot, at present, describe definitely when the linear state, including the initial wavelets, is transformed to the nonlinear state represented by the wind waves in their statistically stationary state. However, it is inferred from the discussion in the foregoing paragraph that the transition corresponds to the above-mentioned visual change of the surface state. We can point out another fact which supports the inference. In their photograph 2 Toba *et al.* (1975) presented a sequence of photographs which demonstrates the process whereby neutral particles, which were placed just beneath the water surface, are quickly dispersed into water after the start of the wind. We may see from the photographs that the time when the surface state changes visually corresponds to the time when the neutral particles just start to disperse downward into the water. Since this implies that the turbulent motion in the water, characterizing the stationary wind waves, commences simultaneously with the visual change of the surface state, it also supports the above inference. A more detailed description of the experiment and the photograph itself are referred to in their original paper. These studies are also briefly discussed in a review paper by Toba (1978*b*).

In conclusion, the generation of initial wavelets can be well explained by the linear instability theory, but they last for only about 10 s, and the phenomena of wind waves are inferred to be inherently nonlinear, throughout almost all their lives after the short duration of the initial wavelets. The linear instability mechanism was proposed to explain the generation of turbulence, in theoretical studies of the breakdown of a shear flow, for example, while in the study of wind waves the same mechanism has been discussed to explain the growth process of these waves. However, the present study reveals that the linear instability mechanism should be considered as the generation mechanism also for wind waves.

This paper is the essential part of the author's Ph.D. dissertation (Kawai 1977*b*). The author expresses his deep thanks to Professor Y. Toba and Mr K. Okuda of Tohoku University for sharing physical insight. The computation contained in the present article was performed by use of ACOS–NEAC–700 at Computer Center of Tohoku University. This study was partially supported by the Grant-in-Aid for Scientific Research Project nos. 942004 and 254114, by the Ministry of Education, Science and Culture.

Appendix A

There exists a serious problem in the direct integration method for solving the Orr–Sommerfeld equation. Due to large Reynolds number, a large difference in the rate of change of the solution along the y direction, between the viscous mode and the inviscid mode, makes the numerical integration difficult (e.g. Betchov & Criminale, 1967). If the Runge–Kutta numerical integration method is simply applied, the inviscid mode of the solution ϕ_β would be contaminated by the viscous mode ϕ_γ in certain steps of integration, say

$$\bar{\phi}_\beta = \phi_\beta + \lambda \phi_\gamma, \tag{A 1}$$

where $\bar{\boldsymbol{\Phi}}_\beta$ is the inviscid mode contaminated by the viscous mode and λ is a scalar value, because the numerical errors in the inviscid mode increase with the rate of increase of the viscous mode which is far greater than that of the inviscid mode. It should be noted here that the vector form $\boldsymbol{\Phi}$ of the solution consists of zeroth to third differential coefficients of the solution ϕ. Although the general solution is represented by a linear combination of $\bar{\boldsymbol{\Phi}}_\beta$ and $\boldsymbol{\Phi}_\gamma$ when λ is still relatively small, the situation reverses itself when λ becomes large. In our problems, $\bar{\boldsymbol{\Phi}}_\beta$ becomes parallel to $\boldsymbol{\Phi}_\gamma$ before the integration reaches to the interface unless some adequate measures are taken. To overcome this problem, a modified form of Kaplan's (1964) filtered method is used in the present study, which filters out the viscous mode from the contaminated inviscid mode $\bar{\boldsymbol{\Phi}}_\beta$. The name of the method is after the classification by Gersting & Jankowski (1972) who reviewed the numerical schemes to solve the Orr–Sommerfeld equation.

To estimate the magnitude of a certain mode contained in a solution, some preparations are necessary according to Betchov & Criminale (1967). Let's first consider the differential equation

$$(U-c)(\phi''-k^2\phi)-U''\phi=(ikRe)^{-1}(\phi^{\mathrm{iv}}-2k^2\phi''+k^4\phi) \tag{A 2}$$

which is the general form of (4.2) and (4.3). When the coefficients in the equation are constant, it can be solved analytically and the independent particular solutions $\tilde{\phi}_i$'s are as follows:

$$\left.\begin{aligned}\tilde{\phi}_1&=\exp(\gamma y), \quad \tilde{\phi}_2=\exp(-\gamma y),\\ \tilde{\phi}_3&=\exp(\beta y), \quad \tilde{\phi}_4=\exp(-\beta y),\end{aligned}\right\} \tag{A 3}$$

where

$$\left.\begin{aligned}\gamma^2&=k^2+ikRe(U-c), \quad \mathrm{Re}(\gamma)>0,\\ \beta^2&=k^2+U''/(U-c), \quad \mathrm{Re}(\beta)>0,\end{aligned}\right\} \tag{A 4}$$

for sufficiently large Reynolds number Re, where Re represents the real part. A solution ϕ is represented by a linear combination of the particular solutions, say

$$\phi=\sum_{i=1}^{4} a_i\tilde{\phi}_i \tag{A 5}$$

where a_i's are the coefficients of linear combination. Substituting (A 3) into (A 5), and solving them for a_i's, they are

$$\left.\begin{aligned}a_1&=\frac{-\exp(-\gamma y)}{2\gamma(\beta^2-\gamma^2)}(\phi'''+\gamma\phi''-\beta^2\phi'-\gamma\beta^2\phi),\\ a_2&=\frac{\exp(\gamma y)}{2\gamma(\beta^2-\gamma^2)}(\phi'''-\gamma\phi''-\beta^2\phi'+\gamma\beta^2\phi),\\ a_3&=\frac{\exp(-\beta y)}{2\beta(\beta^2-\gamma^2)}(\phi'''+\beta\phi''-\gamma^2\phi'-\beta\gamma^2\phi),\\ a_4&=\frac{-\exp(\beta y)}{2\beta(\beta^2-\gamma^2)}(\phi'''-\beta\phi''-\gamma^2\phi'+\beta\gamma^2\phi).\end{aligned}\right\} \tag{A 6}$$

The relations show that the magnitude a_i's of the individual particular solution in (A 3) contained in a solution ϕ can be estimated from the zeroth to third differential coefficient of the solution. Although the coefficients in the equation (A 2) are not

constant in general, they are assumed constant locally according to Betchov & Criminale (1967).

In the actual purification procedures, a_2 for the solution in the air and a_1 for the solution in the water are used to estimate the magnitude, say $A(\boldsymbol{\phi})$, of the viscous mode contained in a certain solution, say $\boldsymbol{\phi}$, where the values of γ and β are computed from (A 4) with local values of U and U'' at the point considered. As the magnitude of the viscous mode in the inviscid mode must be zero,

$$A(\boldsymbol{\phi}_\beta) = 0. \tag{A 7}$$

Substituting (A 1) into (A 7), the scalar value λ is solved as

$$\lambda = \frac{A(\boldsymbol{\phi}_\beta)}{A(\boldsymbol{\phi}_\gamma)}, \tag{A 8}$$

then the purified solution of the inviscid mode is given from (A 1), as

$$\boldsymbol{\phi}_\beta = \bar{\boldsymbol{\phi}}_\beta - \frac{A(\bar{\boldsymbol{\phi}}_\beta)}{A(\boldsymbol{\phi}_\gamma)}\boldsymbol{\phi}_\gamma. \tag{A 9}$$

Appendix B

If the two independent particular solutions $\boldsymbol{\phi}_{a\gamma}$, $\boldsymbol{\phi}_{a\beta}$ in the air and two $\boldsymbol{\phi}_{w\gamma}$, $\boldsymbol{\phi}_{w\beta}$ in the water, each of which fulfils the boundary conditions at infinity, have been solved under a trial eigenvalue, then the error in the eigenvalue is estimated as follows. General solutions $\boldsymbol{\phi}_w$ in the water and $\boldsymbol{\phi}_a$ in the air are represented by these particular solutions, as

$$\left.\begin{aligned} \boldsymbol{\phi}_w &= X_1\boldsymbol{\phi}_{w\gamma} + X_2\boldsymbol{\phi}_{w\beta} \\ \text{and} \quad \boldsymbol{\phi}_a &= X_3\boldsymbol{\phi}_{a\gamma} + X_4\boldsymbol{\phi}_{a\beta}, \end{aligned}\right\} \tag{B 1}$$

respectively, where X_i's are scalar coefficients of linear combination. Substituting the values of (B 1) at $y = 0$ into the interfacial boundary conditions (4.5)–(4.8), four linear algebraic equations for X_i's are obtained, and they are represented in a matrix form as

$$[A_{ij}]\{X_j\} = \{0\}, \tag{B 2}$$

where all components A_{ij} of the matrix are represented by known values. The determinant of the matrix must be zero, that is

$$|A_{ij}| = 0, \tag{B 3}$$

for non-trivial solutions $\{X_j\}$ to exist. For a trial eigenvalue c, in general, the determinant is not equal to zero and a residual value ϵ exists as

$$|A_{ij}(c)| = \epsilon, \tag{B 4}$$

where c and ϵ are complex variables, and ϵ is zero for the true eigenvalue. The problem of finding the root of the complex variable equation is solved with a trial and error method.

REFERENCES

AKAIKE, H. 1969 Power spectrum estimation through autoregressive model fitting. *Ann. Inst. Statist. Math.* **21**, 407–419.

AKAIKE, H. 1970 Statistical predictor identification. *Ann. Inst. Statist. Math.* **22**, 203–217.

AKAIKE, H. & NAKAGAWA, T. 1972 *Statistical Analysis and Control of Dynamic Systems.* Tokyo: Saiensu-Sha Press (in Japanese).

BENJAMIN, T. B. 1963 The threefold classification of unstable disturbances in flexible surfaces bounding inviscid flows. *J. Fluid Mech.* **16**, 436–450.

BETCHOV, R. & CRIMINALE, W. O. 1967 *Stability of Parallel Flows.* New York: Academic Press.

BURG, J. P. 1967 Maximum entropy spectral analysis. *Paper presented at the 37th Ann. Int. Meet., Soc. Explor. Geophys., Oklahoma City.*

FLECK, J. T. & FRYER, W. D. 1953 An exploration of numerical filtering techniques. *Cornell Aero. Lab., Inc., Rep.* no. XA-869-P-1.

GASTER, M. 1962 A note on the relation between temporally-increasing and spatially-increasing disturbances in hydrodynamic stability. *J. Fluid Mech.* **14**, 222–224.

GERSTING, J. M. & JANKOWSKI, D. F. 1972 Numerical methods for Orr–Sommerfeld problems. *Int. J. Num. Methods Engng* **4**, 195–206.

HIDY, G. M. & PLATE, E. J. 1966 Wind action on water standing in a laboratory channel. *J. Fluid Mech.* **26**, 651–687.

KAPLAN, R. E. 1964 The stability of laminar incompressible boundary layers in the presence of compliant boundaries. *Mass. Inst. Tech. Aeroelastic & Structures Res. Lab.*, ASRL-TR 116–1.

KAWAI, S. 1977*a* On the generation of wind waves relating to the shear flow in water – A preliminary study. *Sci. Rep. Tohoku Univ.* (5), *Geophys.* **24**, 1–17.

KAWAI, S. 1977*b* On the generation of wind waves. Ph.D. Dissertation, Tohoku Univ.

KUNISHI, H. 1957 Studies on wind waves with use of wind flume. (I) On the shearing flow in the surface boundary layer caused by wind stress. *Ann. Disas. Prev. Res. Inst., Kyoto Univ.* **1**, 119–127 (in Japanese).

KUNISHI, H. 1959 On design of resistive wave meter. *Ann. Disas. Prev. Res. Inst., Kyoto Univ.* **3**, 65–73 (in Japanese).

KUNISHI, H. 1963 An experimental study on the generation and growth of wind waves. *Disas. Prev. Res. Inst., Kyoto Univ., Bull.* no. 61.

LANDAU, L. D. & LIFSHITZ, E. M. 1959 *Fluid Mechanics* (English edition). Pergamon Press.

LARNAES, G. 1976 Formation of wind waves. *Tech. Univ. Denmark, Inst. Hydrody. & Hydraul. Engng Series* paper 10.

LARSON, T. R. & WRIGHT, J. W. 1975 Wind-generated gravity-capillary waves: laboratory measurements of temporal growth rates using microwave backscatter. *J. Fluid Mech.* **70**, 417–436.

LOCK, R. C. 1954 Hydrodynamic stability of the flow in the laminar boundary layer between parallel streams. *Proc. Camb. Phil. Soc.* **50**, 105–124.

MILES, J. W. 1957*a* On the generation of surface waves by shear flows. *J. Fluid Mech.* **3**, 185–204.

MILES, J. W. 1957*b* On the velocity profile for turbulent flow near a smooth wall. *J. Aero. Sci.* **24**, 704.

MILES, J. W. 1960 On the generation of surface waves by turbulent shear flows. *J. Fluid Mech.* **7**, 469–478.

MILES, J. W. 1962 On the generation of surface waves by shear flows. Part 4. *J. Fluid Mech.* **13**, 433–448.

MITSUYASU, H. & HONDA, T. 1974 The high frequency spectrum of wind-generated waves. *J. Oceanog. Soc. Japan* **30**, 185–198.

MONIN, A. S. & YAGLOM, A. M. 1971 *Statistical Fluid Mechanics* (English edition), vol. 1, MIT Press, Mass., 769 pp.

OKUDA, K., KAWAI, S. TOKUDA, M. & TOBA, Y. 1976 Detailed observation of the wind-exerted surface flow by use of flow visualization methods. *J. Oceanog. Soc. Japan* **32**, 53–64.

OKUDA, K., KAWAI, S. & TOBA, Y. 1977 Measurement of skin friction distribution along the surface of wind waves. *J. Oceanog. Soc. Japan* **33**, 190–198.

PHILLIPS, O. M. 1957 On the generation of waves by turbulent wind. *J. Fluid Mech.* **2**, 417–445.

PLANT, W. J. & WRIGHT, J. W. 1977 Growth and equilibrium of short gravity waves in a wind-wave tank. *J. Fluid Mech.* **82**, 767–793.

PLATE, E. J., CHANG, P. C. & HIDY, G. M. 1969 Experiments on the generation of small water waves by wind. *J. Fluid Mech.* **35**, 625–656.

SCHUBAUER, G. B. & SKRAMSTAD, H. K. 1947 Laminar boundary-layer oscillations and stability of laminar flow. *J. Aero Sci.* **14**, 69–78.

SHEMDIN, O. H. 1972 Wind-generated current and phase speed of wind waves. *J. Phys. Oceanog.* **2**, 411–419.

SNYDER, R. L. & COX, C. S. 1966 A field study of the wind generation of ocean waves. *J. Mar. Res.* **24**, 141–178.

STEWART, R. W. 1974 The air–sea momentum exchange. *Boundary-Layer Met.* **6**, 151–167.

TOBA, Y. 1978*a* Stochastic form of the growth of wind waves in a single-parameter representation with physical interpretation. *J. Phys. Oceanog.* **8**, 494–507.

TOBA, Y. 1978*b* Study on wind waves as a strongly nonlinear phenomenon. To be published in *Proc. 12th Symp. Naval Hydrodyn. Nat. Acad. Sci., Washington D.C.*

TOBA, Y., TOKUDA, M., OKUDA, K. & KAWAI, S. 1975 Forced convection accompanying wind waves. *J. Oceanog. Soc. Japan* **31**, 192–198.

TURNER, J. S. 1973 *Buoyancy Effects in Fluids.* Cambridge University Press.

ULRYCH, T. J. & BISHOP, T. N. 1975 Maximum entropy spectral analysis and autoregressive decomposition. *Rev. Geophys. Space Phys.* **13**, 183–200.

VALENZUELA, G. R. 1976 The growth of gravity-capillary waves in the coupled shear flow. *J. Fluid Mech.* **76**, 229–250.

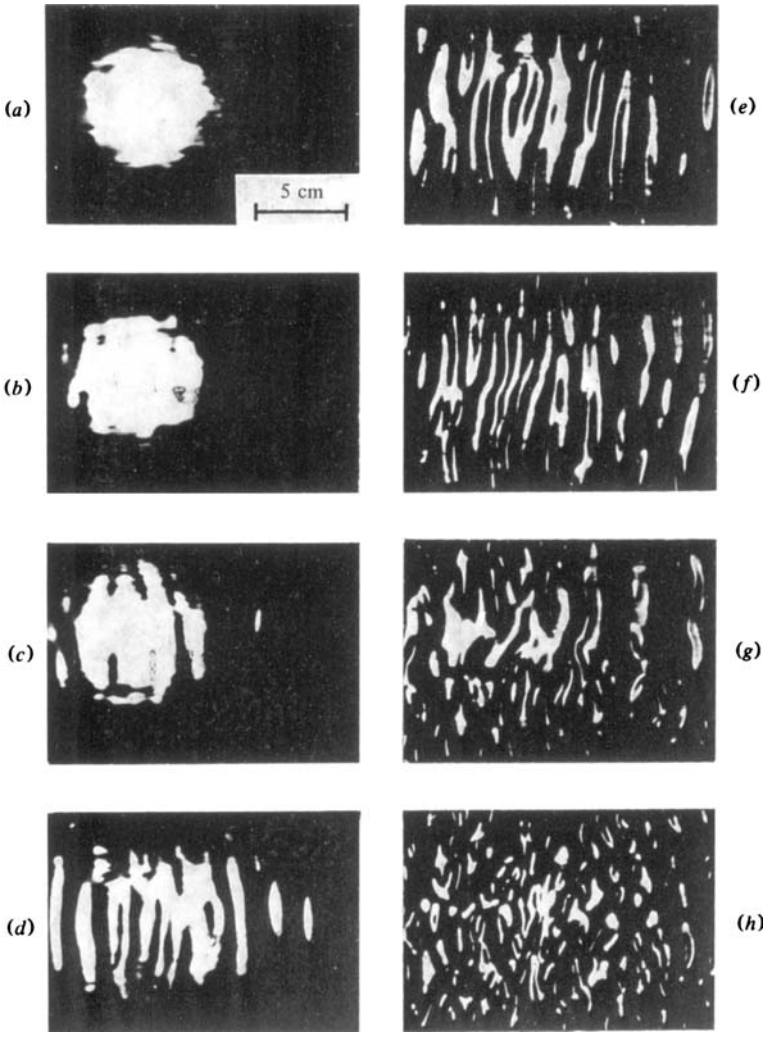

FIGURE 1. A sequence of photographs of the water surface taken after the start of the wind at 0·6 s intervals by a camera facing vertically downward. The wind was 6·3 m s^{-1}, from the left to the right of each picture. The white circles seen in the earlier pictures are the images of a stroboscope. The distinction between the initial wavelets (*c*) to (*f*) and the later wind waves (*h*) is clearly seen. The times measured in seconds from the start of the wind are: (*a*) 3·66; (*b*) 4·24; (*c*) 4·84; (*d*) 5·42; (*e*) 6·01; (*f*) 6·60; (*g*) 7·20; (*h*) 7·80.